AGU PUBLICATIONS

Geochemistry, Geophysics, Geosystems

RESEARCH ARTICLE
10.1002/2015GC005928

Key Points:
- Active mud volcanoes expel methane on the continental slope of the Beaufort Sea
- Methane supports chemosynthetic communities and near seafloor gas hydrate formation
- Venting fluid reflects meteoric sea water, and smectite/illite end-members

Supporting Information:
- Supporting Information S1
- Table S1
- Table S2

Correspondence to:
C. K. Paull,
Paull@MBARI.org

Citation:
Paull, C. K., et al. (2015), Active mud volcanoes on the continental slope of the Canadian Beaufort Sea, *Geochem. Geophys. Geosyst.*, *16*, 3160–3181, doi:10.1002/2015GC005928.

Received 26 MAY 2015
Accepted 1 SEP 2015
Accepted article online 4 SEP 2015
Published online 24 SEP 2015

Active mud volcanoes on the continental slope of the Canadian Beaufort Sea

C. K. Paull[1], S. R. Dallimore[2], D. W. Caress[1], R. Gwiazda[1], H. Melling[3], M. Riedel[2], Y. K. Jin[4], J. K. Hong[4], Y.-G. Kim[4], D. Graves[1], A. Sherman[1], E. Lundsten[1], K. Anderson[1], L. Lundsten[1], H. Villinger[5], A. Kopf[6], S. B. Johnson[1], J. Hughes Clarke[7], S. Blasco[8], K. Conway[2], P. Neelands[2], H. Thomas[1], and M. Côté[2]

[1]Monterey Bay Aquarium Research Institute, Moss Landing, California, USA, [2]Geological Survey of Canada, Sidney, British Columbia, Canada, [3]Department of Fisheries and Oceanography, Institute of Ocean Sciences, Sidney, British Columbia, Canada, [4]Korea Polar Research Institute, Incheon, South Korea, [5]Department of Geosciences, Universary of Bremen, Bremen, Germany, [6]Center for Marine Environmental Sciences, Universary of Bremen, Bremen, Germany, [7]University of New Brunswick, Fredericton, Canada, [8]Geological Survey of Canada, Halifax, Nova Scotia, Canada

Abstract Morphologic features, 600–1100 m across and elevated up to 30 m above the surrounding seafloor, interpreted to be mud volcanoes were investigated on the continental slope in the Beaufort Sea in the Canadian Arctic. Sediment cores, detailed mapping with an autonomous underwater vehicle, and exploration with a remotely operated vehicle show that these are young and actively forming features experiencing ongoing eruptions. Biogenic methane and low-chloride, sodium-bicarbonate-rich waters are extruded with warm sediment that accumulates to form cones and low-relief circular plateaus. The chemical and isotopic compositions of the ascending water indicate that a mixture of meteoric water, seawater, and water from clay dehydration has played a significant role in the evolution of these fluids. The venting methane supports extensive siboglinid tubeworms communities and forms some gas hydrates within the near seafloor. We believe that these are the first documented living chemosynthetic biological communities in the continental slope of the western Arctic Ocean.

1. Introduction

Multibeam bathymetric mapping surveys conducted in 2009 and 2010 by the ArcticNet project in collaboration with Canadian industry provided the first detailed bathymetry for a 100 km long section of the shelf edge and slope of the Canadian Beaufort Sea (see http://www.omg.unb.ca/Projects/Arctic/google/ for data catalog). These data revealed the existence of five circular morphologic features, in water depths of ~282 m, ~420 m, and a cluster of three closely spaced structures in ~740 m water depth (Figures 1 and 2). These features are henceforth designated by their water depths. Water column acoustic anomalies were identified over each of these features, indicating that they are sites of active gas venting and thus initially interpreted as being large mud volcanoes [*Blasco et al.*, 2013; *Saint-Ange et al.*, 2014]. These five features became the target of focused investigations to document the seafloor environment, determine the nature of the venting fluids, and evaluate the eruptive activity.

1.1. Mud Volcanoes

Mud volcanoes are the sediment buildups associated with the extrusion of gas and water-saturated fine-grained sediment [e.g., *Milkov*, 2000; *Dimitrov*, 2002; *Kopf*, 2002]. They occur in both marine and terrestrial environments and are thought to be most common in settings where there is significant compressional stress and rapid sediment accumulation. There are large variations in the size and geometries as well as the sources of the fluids and sediments that are expelled by mud volcanoes. Biogenic or thermogenic hydrocarbon gases and pore waters of highly evolved compositions, indicating extensive water-rock interactions [e.g., *Li et al.*, 2014], are frequently observed in such features. Mud volcanoes can have discrete eruptive events or periods of eruption that expel massive quantities of fine-grained sediments in periods of hours to centuries [*Zoporowski and Miller*, 2009].

Mud volcanoes and other sites on the seafloor where hydrocarbon venting occurs have attracted considerable attention from the research community, as they frequently host gas hydrate deposits within the

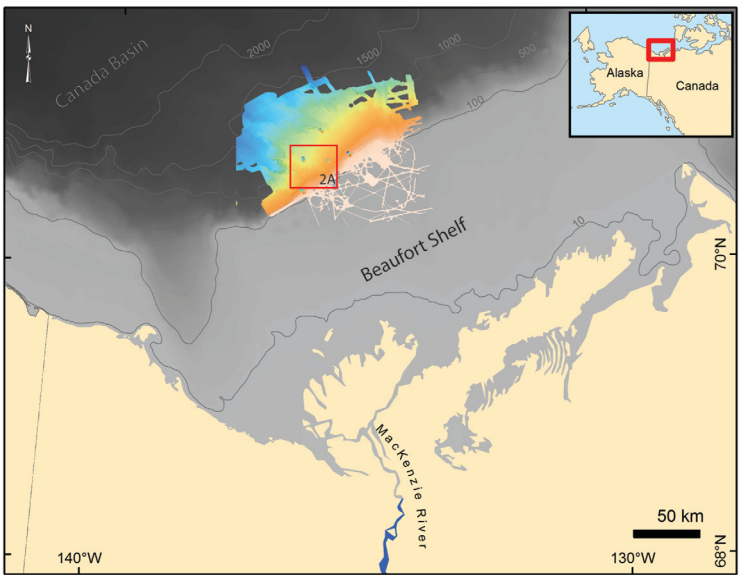

Figure 1. Map showing location of ArcticNet multibeam surveys (colored bathymetry) conducted on the shelf edge and continental slope of the Canadian Beaufort Sea [*Saint-Ange et al.*, 2014] with respect to the Mackenzie River, Beaufort Shelf, and Canada Basin. Inset map shows location with respect to Alaska and northwestern Canada. Area covered in more detail in Figure 2a is indicated with red box. Contours at 10, 100, 500, 1000, 1500, and 2000 m.

sediments near the seafloor, support chemosynthetic biological communities, and affect the stability of the surrounding seafloor [e.g., *Lösekann et al.*, 2008; *Feseker et al.*, 2009a, 2009b, 2014]. Individual mud volcano eruptions can emit relatively large amounts of methane. While the total number of mud volcanoes and their average eruption frequency is still poorly constrained, the methane flux from mud volcanoes is estimated to be 3–5% of the natural methane input to the atmosphere [*Etiope and Milkov*, 2004]. Moreover, the flux of carbon from mud volcanoes (both methane and bicarbonate) is unknown.

1.2. Geologic Setting

The continental slope of the Canadian Beaufort Sea separates the 100 km wide Beaufort Shelf from the Canada Basin to the north (Figure 1). This slope has remained poorly explored, in part because the extensive cover of sea ice makes access difficult. The slope and adjacent continental shelf are underlain by up to 12 km thick sedimentary sequence composed of Mesozoic to Quaternary strata [*Cook et al.*, 1987; *Dixon*, 1993; *Grantz and Hart*, 2012], with the Mackenzie River presently supplying 124×10^6 ton of sediment per year to this margin [*Holmes et al.*, 2002].

The Quaternary section on the shelf is composed of unconsolidated transgressive/regressive sands, silts, and clay horizons that are largely horizontally bedded [*Blasco et al.*, 1990]. Less is known of the geology of the slope areas; however, industry seismic data seem to indicate a much more complex stratigraphy with thick sediment packages including deformed sediments. Numerous industry exploration wells drilled on the shelf mainly in the 1970s and 1980s revealed that the Quaternary shelf sediments contain ice bonded permafrost down to 700 m and gas hydrate to depths of 1200 m below seafloor [*Weaver and Stewart*, 1982; *Pelletier*, 1987; *Taylor et al.*, 2013]. The present water column of the Beaufort Sea is stratified with an upper layer of cold water (i.e., minimum temperature of -1.5°C) which extends from the base of the seasonal thermocline ($\gtrsim$30 m) down to $\sim$200 m and then warms to a maxima of over 0.5°C at $\sim$350 m [*McLaughlin et al.*, 2004].

2. Methods

Cruises were conducted in the fall of 2010 (2010-035-WD), 2012 (2012004PGC), and 2013 (2013005PGC) on the Canadian Coast Guard Icebreaker *Sir Wilfred Laurier* (*SWL*) and in the fall of 2013 (ARA04C) and 2014 (ARA05C) on the South-Korean Icebreaker *Araon* to investigate the shelf edge and slope of the Canadian Beaufort Sea. The methods of investigation include sediment coring, detailed mapping with an autonomous underwater vehicle (AUV), and exploration with a remotely operated vehicle (ROV).

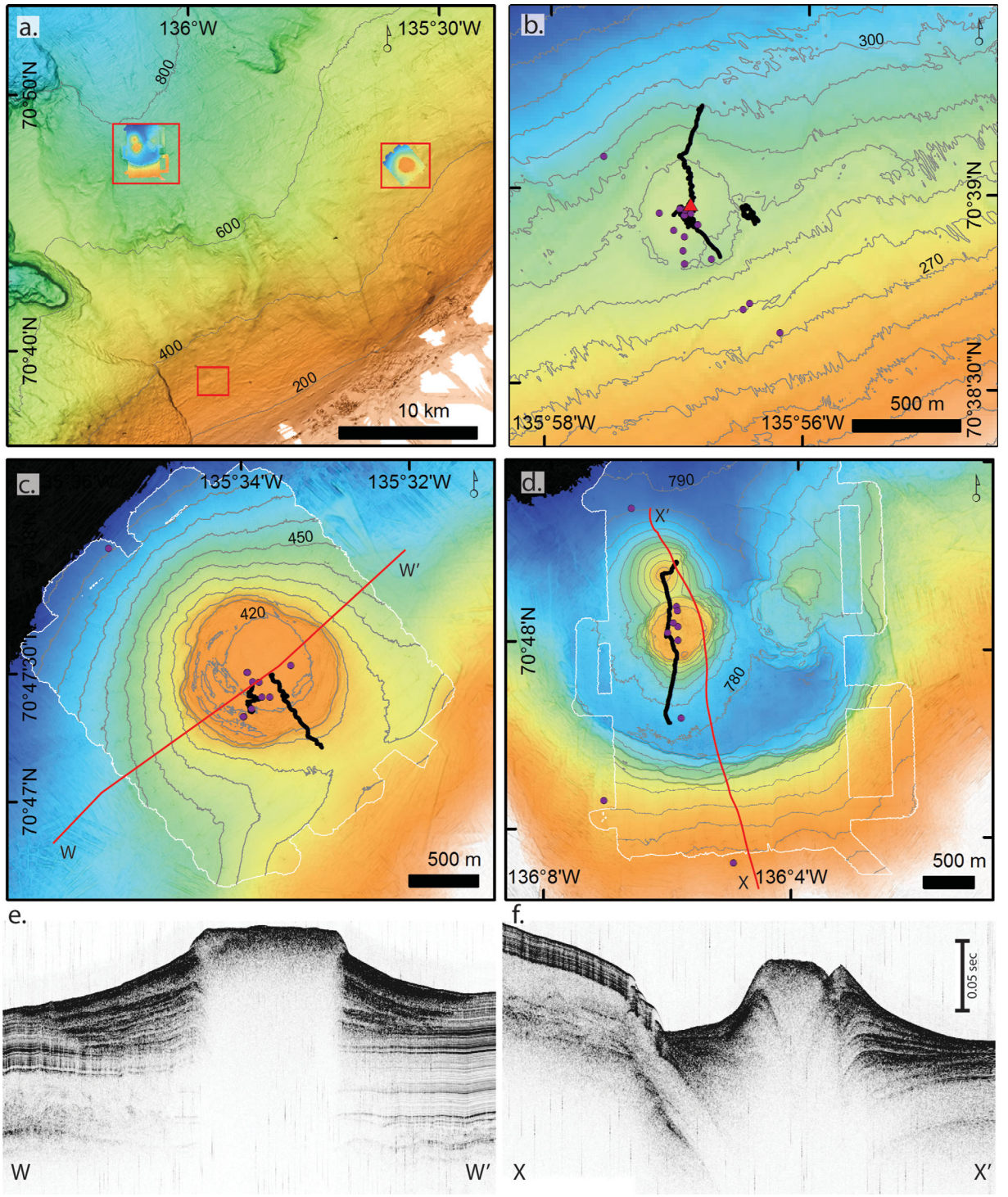

Figure 2. Maps showing locations of sampling of three areas containing large mud volcanoes on the slope of the Beaufort Sea. Background bathymetry is ArticNet multibeam [*Saint-Ange et al.*, 2014] with AUV data superimposed in Figures 2a, 2c, and 2d outlined in white. Figure 1 indicates area covered in Figure 2a. Figure 2a shows location of three areas of mud volcanoes shown in more detail in Figures 2b–2d. Figure 2b shows a feature in ~282 m water depth surveyed in surface ship multibeam only. Figure 2c shows single flat-topped mud volcano at ~420 m water depth, which is elevated ~10 m with respect to the surrounding seafloor. Figure 2d shows a cluster of three mud volcanoes in ~740 m water depths, one flat-topped, one conical, and one irregular. Location of sediment cores and ROV dive transects are identified with purple circles and black circles, respectively. Mooring at ~282 m is indicated with a red triangle. Contour intervals are 200 m in Figure 2a and 5 m in Figures 2b–2d. High-resolution seismic profiles collected by the *Araon* crossing the (e) ~740 m and (f) ~420 m features. Locations of profiles shown in E (W-W') and F (X-X') are the red lines in Figures 2c and 2d, respectively. Vertical exaggerations are ~90.

Table 1. Percent Contribution of Major Gases, Stable Isotopic Composition of Methane, and ^{14}C Content of Methane Collected From Beaufort Sea Expulsion Features[a]

Cruise	Station	Sample Name	C_1 (%)	C_2 (%)	C_3 (%)	C_1/C_2 (%)	$\delta^{13}C_1$ (‰)	δDC_1 (‰)	$\delta^{13}C_2$ (‰)	$^{14}C_1$ (pmC)	SD
2013005PGC	STN077	GC-25-1	93.45	0.121	nd	772	−65.63	−226.2			
2013005PGC	STN077	GC-25-2	93.38	0.119	6E-04	785	−65.74	−227.7			
2013005PGC	STN078	GC-26	78.47	0.058	7E-04	1353	−63.62	−220.8			
2012004PGC	Dive 8	420 m ROV	94.91	0.0156	0.0009	6084	−64.85	−219.5		0.5	0.1
2012004PGC	STN003	PC-001-3	0.467	0.0008	nd	584	−64.8	−216			
2012004PGC	STN017	PC-003-1	94.18	0.0454	0.0007	2074	−64.93	−223.3	−49.2		
2012004PGC	STN017	PC-003-2	97.44	0.0422	0.0006	2309	−65.14	−224.7	−49.4		
2012004PGC	STN023	PC-005-3	93.51	0.0455	0.0012	2055	−64.90	−233.4	−47.4		

[a]nd = not detected.

2.1. Core Sampling

Sediments from the five circular seafloor structures that occur within the study area and from the undisturbed slope at equivalent depths were sampled with 5 piston cores, 34 gravity cores, and a multicorer (Figure 2 and supporting information Table S1). Twenty-nine of these cores were from the circular features and 11 were background cores from the continental slope. Piston cores up to 716 cm long and gravity cores up to 425 cm long were recovered.

Upon recovery, most of the cores from the circular structures were observed to expand and bubble profusely. Gas samples from core voids were taken by inserting a thick needle through the plastic core liner to withdraw gas into a syringe [after *Claypool et al*., 1973]. Gas was then transferred underwater into gas-tight bottles and sealed. Gas samples were analyzed for composition and methane $\delta^{13}C$, δD, and ^{14}C by Isotech Laboratories, Champaign, Illinois, USA (Table 1).

Immediately after the cores were capped and labeled, holes were drilled at 10–35 cm spacing down the core liner and pore water was extracted using rhizon samplers [*Dickens et al*., 2007] connected to 10 mL syringes. Pore water samples were refrigerated until analysis. Major cation and anion concentrations were determined by ion chromatography at the Monterey Bay Aquarium Research Institute (MBARI) following techniques of *Ussler and Paull* [2007]. Precision is estimated to be better than 1% for chloride and sulfate, but decreases at low concentrations. Carbonate alkalinity ($HCO_3^- + 2 \times CO_3^{-2}$) was determined via Gran titration. No corrections were applied to measured carbonate alkalinity concentrations for the possible presence of HS^- or for precipitation of calcium carbonate [*Schrum et al*., 2012]. The $\delta^{18}O$ and δD of pore water samples were measured by Isotech Laboratories.

The *SWL* cores were sealed onboard and returned to the Pacific Geosciences Center (PGC) in Sidney, British Columbia, where they were split, described, and sampled. Some of the 2013 *Araon* cores were split and described shipboard, while others were returned to PGC for splitting and description. All the 2014 *Araon* cores were processed at sea.

Thermal gradients were measured in two manners: (1) using three to five temperature loggers attached 50 cm apart as outriggers on the side of 2.5–4 m long gravity corer from the *SWL* [*Riedel et al*., 2014] and (2) using a Lister-type heat probe whose length is 5 m and has eight thermistors attached 30–80 cm apart as outriggers [*Jin et al*., 2015]. After penetration, the core and the heat probe were left undisturbed for 7 and 20 min, respectively, on average. Ground temperatures were estimated by extrapolating to infinite time.

2.2. ROV Dives

An inspection class ROV was built for this field program by Dale Graves and Alana Sherman at MBARI. The vehicle carried an Insite Nova Camera, a Falmouth Scientific Instruments (FSI) Micro CTD, and an obstacle avoidance sonar (Imagenex Technology, Model 881A). Video observations were recorded onto a Sony HD Video Cam Recorder. Vehicle positions were logged as GPS fixes recorded on the bridge that were in turn corrected to the location of the overboarding sheave. A ~150 kg clump weight was fixed 25 m from the end of the ROV umbilical to keep the tether taut while providing a 25 m radius of operation when on the seafloor. With the additional error associated with the tether catenary, ROV positions are accurate to ±50 m.

Five ROV dives conducted in 2012 focused on exploring and sampling gas from the tops and flanks of three expulsion features (Dives 5, 11, and 12 on the ~282 m feature, Dive 6 on the ~740 m feature, and Dive 8 on

the ~420 m feature). In 2012, the ROV carried a gas collection funnel and sampling system. Gas samples collected by the ROV were analyzed for hydrocarbon gases from C_1 to C_5, methane $\delta^{13}C$ and δD, and ^{14}C content by Isotech Laboratories.

In 2013, only one ROV dive was conducted on the ~420 m feature (Dive 24). In 2013, the addition of a mechanical arm to the ROV allowed a thicket of worms to be sampled. On recovery, the worms were washed in deionized water, photographed, and placed in an −80°C freezer until processed at MBARI. Material from six worms was extracted and amplified for the Cytochrome C oxidase subunit I (COI) mitochondrial DNA locus according to the methods of *Vrijenhoek et al.* [2009]. Sequences were then compared with an existing gene library for organisms that characterize chemosynthetic ecosystems and on GenBank (www.blast.ncbi.nlm.nih.gov). A freeze-dried worm was combusted and the generated CO_2 analyzed for its $\delta^{13}C$ and ^{14}C content by Isotech Laboratories.

Seafloor textures were described from the videotapes recorded during the ROV dives. Visually identifiable benthic fauna were identified to the lowest taxon possible and annotated using MBARI's video annotation reference system, VARS [*Schlining and Stout*, 2006] (http://www.mbari.org/vars/vars_overview.html).

2.3. AUV Mapping Surveys

Detailed seafloor surveys were conducted on the ~420 m (1 and 5 October 2013) and ~740 m (4 October 2013) expulsion features using an AUV developed at MBARI specifically for seafloor mapping [*Caress et al.*, 2008]. The vehicle carried a Reson 7125, 200 kHz 1° by 1° multibeam sonar, an Edgetech 1–6 kHz chirp subbottom profiler, and an Edgetech 110 kHz side scan. The AUV was preprogrammed to proceed to >50 waypoints during the dives while traveling at 3 knots and maintaining an altitude of 50 m off the seafloor. Track lines were spaced ~150 m apart. In this mode, the AUV obtains overlapping multibeam bathymetric coverage at a vertical resolution of 0.15 m and a horizontal footprint of 0.87 m, and chirp seismic reflection profiles with a vertical resolution of 0.11 m. Initial navigation fixes are obtained from Global Positioning System when the AUV is at the sea surface and subsequently updated with a Kearfott inertial navigation system (INS) and a Doppler velocity log (DVL) when within 100 m of the seafloor. Data processing was done using the open source software package MB-System [*Caress and Chayes*, 1996; *Caress et al.*, 2008].

2.4. Seafloor Observations From Mooring

A multicomponent oceanographic mooring was designed in part with the goal to make time series observations relevant to detecting seafloor gas emanations from the ~282 m feature. The mooring was deployed near the center of the feature at 70°39.0156′N, 135°56.8047′W and operated from 30 September 2012 to 1 October 2013. It supported three CTD sensors (conductivity, temperature, and depth; Sea Bird Inc. SBE37), at elevations of 5.3, 11.7, and 34.6 m above the seafloor to assess whether the varying ocean temperature permits gas hydrate stability at the seabed. A 200 kHz sonar (ASL Environmental Sciences Inc. AWCP5; 1.5° beam width) was suspended down looking from 110 m above the seafloor to detect gas bubbles in the water column. An ambient sound recorder (Multi Electronique Inc. AURAL M2) was positioned at 22 m above seafloor to record sounds linked to the formation of gas bubbles at orifices in the seabed [e.g., *von Deimling et al.*, 2010; *Barnard et al.*, 2015].

3. Results

3.1. Cores

3.1.1. Sediment Texture and Gas Hydrate Presence

The cores from the crest and flanks of the circular topographic structures were composed of homogeneous clay and largely barren of macroscopic fossils. No authigenic carbonate was observed. However, a few isolated rounded quartz pebbles occurred within this matrix. Upon collection, cores from nearly all the circular topographic structures at the three sites were noticeably gas charged. Streams of bubbles were often seen emanating from the core barrels during the core recovery. On deck, sediment spontaneously extruded from the core liners and numerous gas filled gaps developed within the cores, but no strong hydrogen sulfide scent was noted. Some of the core sections were observed to continue to release gas for ~1 h after recovery. As a result, the sediments in most cores exhibited moussey textures (Figure 3a) characteristic of deformation associated with gas expansion [e.g., *Paull and Ussler*, 2001; *Piñero et al.*, 2007]. White veins, less than 1 mm thick, were seen in material extruded from *SWL* STN103 GC-41 from the ~420 m feature in 2013.

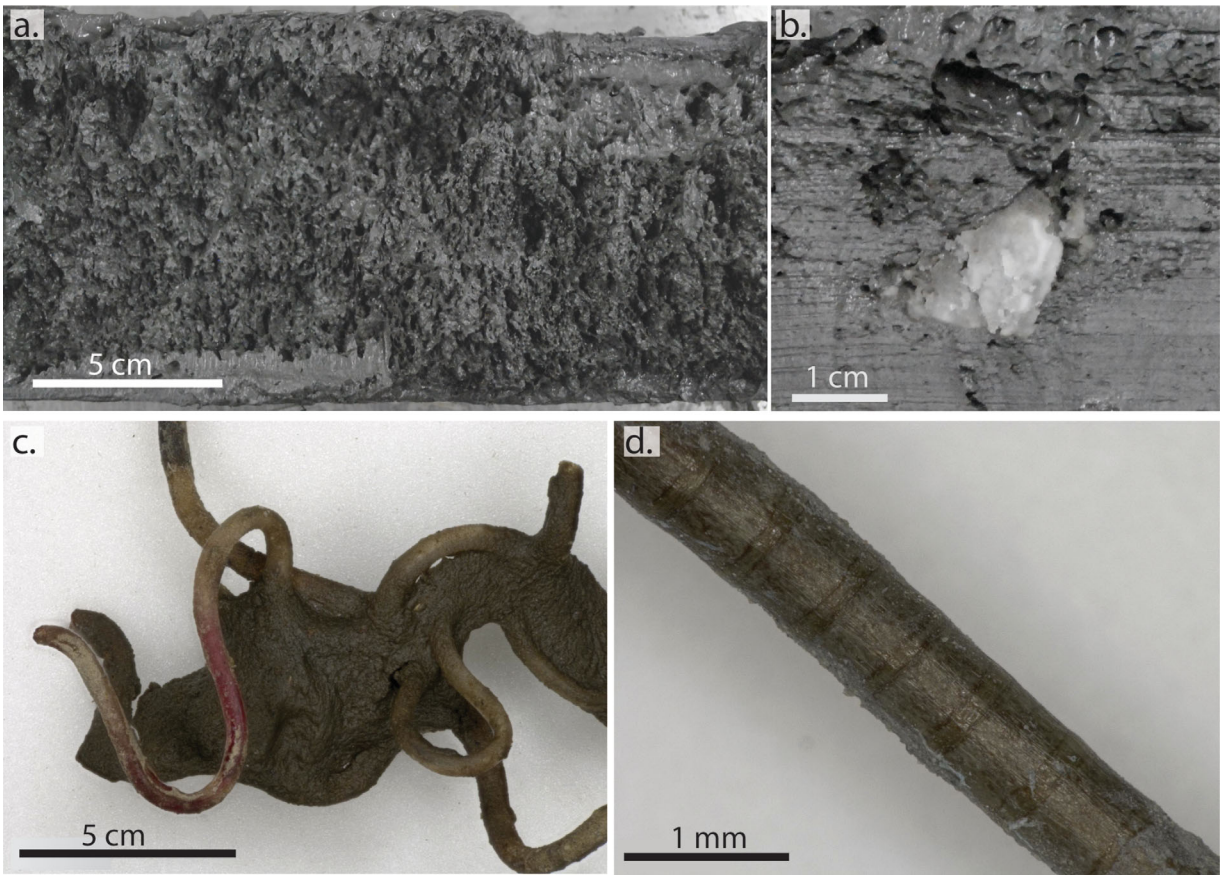

Figure 3. Photograph illustrating core texture, gas hydrate, and tubeworms. (a) Figure 3a illustrates moussey texture characteristic of gas charged and previously gas hydrate-bearing cores. (b) Figure 3b illustrates gas hydrate flake exposed on surface of ARA05C 18GC01 at 230 cmbsf collected at the ~740 m mud volcano. (c) A few interwoven tubeworms collected at the ~420 m mud volcano. (d) Segmented tube of a siboglinid tubeworm.

These were inferred to be gas hydrate because they released gas when touched by hand, and when placed into a syringe a slight volume expansion was noted after the flakes melted at room temperature. Pieces of hydrate were also identified as $\leq$2 cm isolated veins along open cracks between 230 and 300 cmbsf on the face of the freshly split ARA05C 18GC01 core collected from the ~740 m feature (Figure 3b). Background slope cores from depths equivalent to the circular features had limited textural variation and did not display moussey textures.

3.1.2. Gas Composition

The hydrocarbon gas concentrations and isotopic compositions from all three structures are very similar. Methane comprised up to 97% of the gas with secondary amounts of air likely due to sample contamination (Table 1). The C_1 to $C_2 + C_3$ ratios were from 700 to 2200. Hydrocarbon gases higher than C_3 were not detected. Methane in seven samples from the cores yielded a mean $\delta^{13}C$ value of $-64.36‰$ (PDB) and δD values of $-222‰$ (SMOW). The analysis of the gas sample collected by the ROV with the gas funnel at the ~420 m feature ($\delta^{13}C$ $-64.85‰$ (PDB) and δD $-220‰$ (SMOW)) is indistinguishable from the results of the gas collected from the core voids. The ^{14}C content of the methane in the ROV collected gas contained $0.5 \pm 0.1\%$ modern carbon, which we interpret could result from atmospheric contamination as the sample also contained some air (Table 1).

3.1.3. Chemistry of Pore Waters

The pore waters from cores collected on the circular features show steep gradients in chloride and sulfate concentration, from seawater values near the seafloor to unusually low chlorinities ($<$210 m*M*), and sulfate depletion (i.e., $<$0.1 m*M*) typically within 0.5 m below the seafloor (Figures 4a and 4b). These profiles are in sharp contrast with the chloride and sulfate profiles of pore waters from background cores collected on the slope at equivalent depths (Figures 4a and 4b).

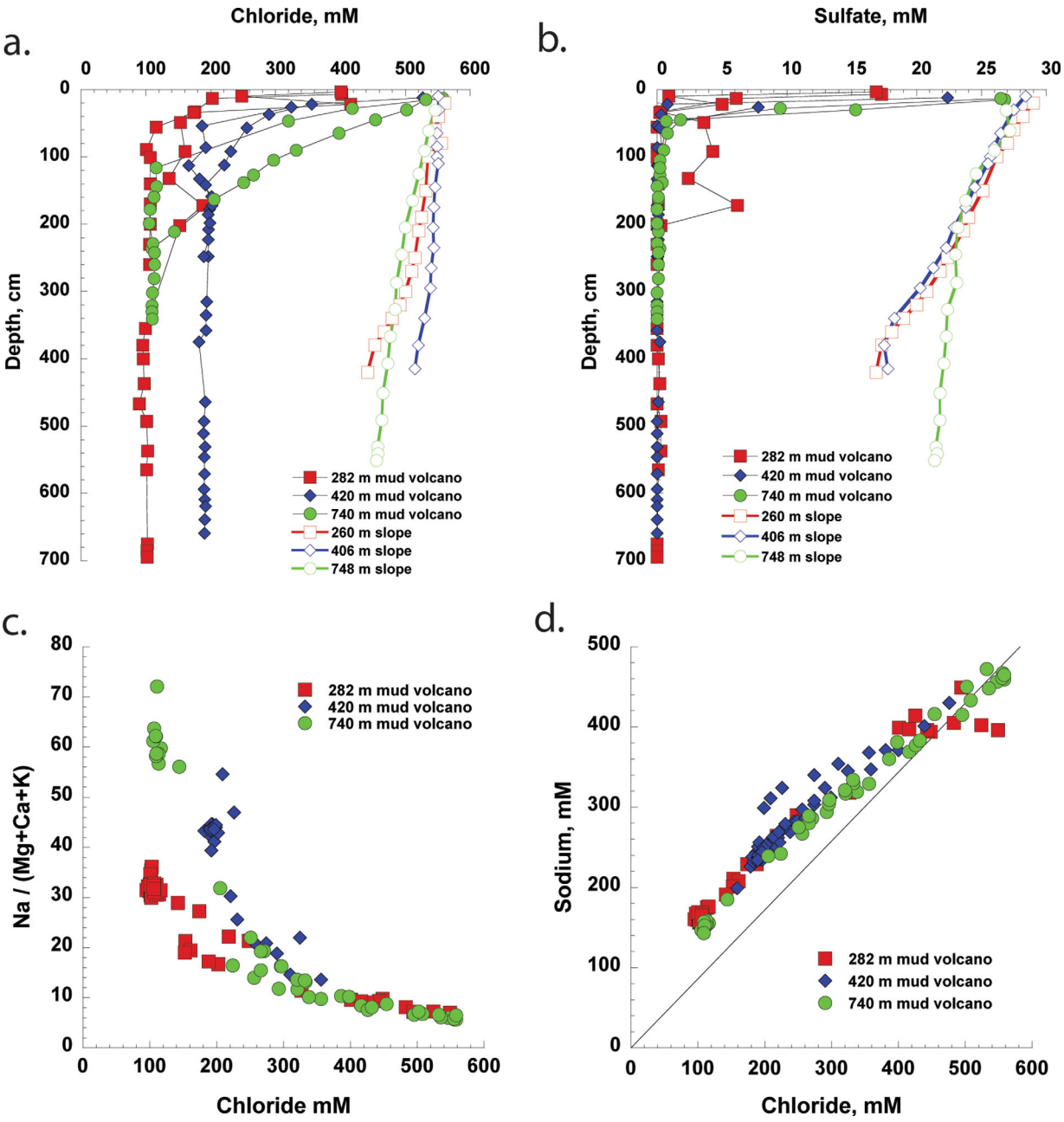

Figure 4. Plots showing pore water characteristics from the top of the ~740, ~420, and ~282 m water depths flat-topped mud volcanoes. (a and b) Pore water chloride and sulfate concentrations for illustrative cores from the ~282, ~420, and ~740 m flat-topped plateaus (filled symbols) and background cores from the slope of equivalent depths (open symbols). The pore waters profiles from these mud volcanoes are distinct from the background cores and show sharp gradients near the seafloor. (c) Ratios of pore waters sodium to sum of magnesium, calcium, and potassium versus chloride concentrations for the three flat-topped plateaus. Note that they converge on different end-member values for each mud volcano. (d) The pore water chloride versus the sodium concentrations. Note waters with lower chloride plot above a mixing line between seawater and freshwater.

Chlorinities in the sulfate-depleted waters stabilize to approximately constant values that define end-member compositions in two to nine cores from each site (Table 2 and Figure 4a). The constant values are $<$125, $<$210, and $\leq$120 m*M* chloride for the ~282, ~420, and ~740 m features, respectively (Figures 4a and 4c). The water end-members are sodium-rich-type waters with depletions in calcium, magnesium, and potassium (Table 2 and Figures 4c, and 4d). Carbonate alkalinity reaches 70 m*M*, a value ~30 times greater than seawater alkalinity. The waters emanating at each feature have different cation ratios, and δ^{18}O and δD values (Table 2 and Figures 4c and 5a). The isotopic compositions of the end-members are significantly displaced from a mixing line between seawater (SMOW: $\delta^{18}O = 0‰$, $\delta D = 0‰$) and meteoric water, as

Table 2. Pore Water Composition of End-Member Samples From Three Mud Volcanoes on the Slope of the Beaufort Sea

	282 m Mud Volcano, Cl <125 m*M*			420 m Mud Volcano, Cl <210 m*M*			740 m Mud Volcano, Cl <120 m*M*			
	Average ± SD	Number of Samples	Number of Cores	Average ± SD	Number of Samples	Number of Cores	Average ± SD	Number of Samples	Number of Cores	Seawater Average
Cl, m*M*	103.7 ± 5.3	33	5	190.9 ± 8.3	52	9	111.1 ± 3.2	14	2	559.4
SO_4, m*M*	0.1 ± 0.1	33	5	0.1 ± 0.2	52	9	0.1 ± 0.1	14	2	28.9
($HCO^{3-} + 2 \times CO_3^{-2}$), meq L^{-1}	69.6 ± 0.8	3	1	53.3 ± 1.5	3	1	43.6 ± 2.1	3	1	2.2
Na, m*M*	164.1 ± 4.7	31	5	241.6 ± 16.7	43	9	151.3 ± 4.5	12	2	480.6
K, m*M*	1.8 ± 0.3	29	5	1.8 ± 0.3	39	9	0.7 ± 0.1	10	2	10.5
Mg, m*M*	3.1 ± 0.2	29	5	3.7 ± 0.5	39	9	1.5 ± 0.1	10	2	54.1
Ca, m*M*	0.3 ± 0.04	29	5	0.6 ± 0.1	39	9	0.4 ± 0.1	10	2	10.5
δD H_2O, ‰	−47.1 ± 1.7	13	5	−40.4 ± 3.7	18	5	−41.2 ± 1.2	7	2	−5.1[a]
$\delta^{18}O$ H_2O, ‰	−3.2 ± 0.2	13	5	−3.9 ± 0.4	18	5	−1.5 ± 0.1	7	2	−0.26[a]

[a]Average values of two water samples collected in the Canadian Beaufort Sea at 406 and 1009 m water depth in August and September 2014.

approximated by the projection of the local meteoric water line, which has a δD intercept of −3.6‰ (Figure 5a).

The background cores on the slope are characterized by gradual downcore decreases in chloride concentrations (Figure 4a). The δ^{18}O values decrease with decreasing chlorinity (Figure 5b). Extrapolation of these gradients indicates that the δ^{18}O values at zero chloride concentration are −19.7‰, −21.8‰, and −22.4‰. The isotopic compositions of the background pore waters lie along the projection of the local meteoric water line, in contrast to the waters collected from the circular features that plot to the right of the local meteoric water line (Figure 5a).

3.1.4. Sediment Temperatures

Transects of thermal measurements were made using temperature loggers attached to the gravity corer across the crests of the ~282, ~420, and ~740 m features. These data consistently show sharp gradients in temperature in the uppermost ~2 m of the seafloor on the flat-topped plateaus and temperatures as high as 9.1°C were measured. The temperature profiles characteristically show linear gradients with variable slopes and gradients of ~2°C or more per meter are typical on these features [*Riedel et al*., 2014; *Jin et al*., 2015]. In comparison, at background sites, a maximum thermal gradient of ~0.08°C per meter was measured using the Lister-type heat probe at ARA05C STN 2 (supporting information Table S1).

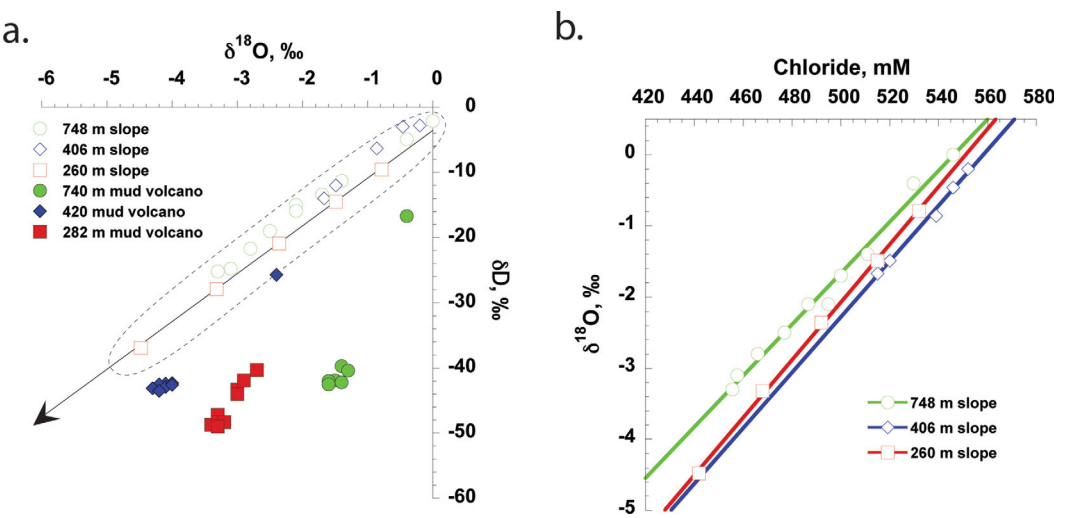

Figure 5. (a) δ^{18}O versus δD values for pore waters collected from the top of the ~740, ~420, and ~282 m water depths flat-topped mud volcanoes and three background cores from 260, 406, and 748 m water depths on the Beaufort Slope (supporting information Tables S1 and S2). The line is a projection of the local meteoric water line for Inuvik, Canada (http://www-naweb.iaea.org/napc/ih/IHS_resources_gnip.html). The background samples are bounded by a dashed black circle and lie along a mixing trend between seawater and meteoric waters. (b) δ^{18}O values versus chloride concentration in background cores, from water depths similar to those of the flat-topped mud volcanoes.

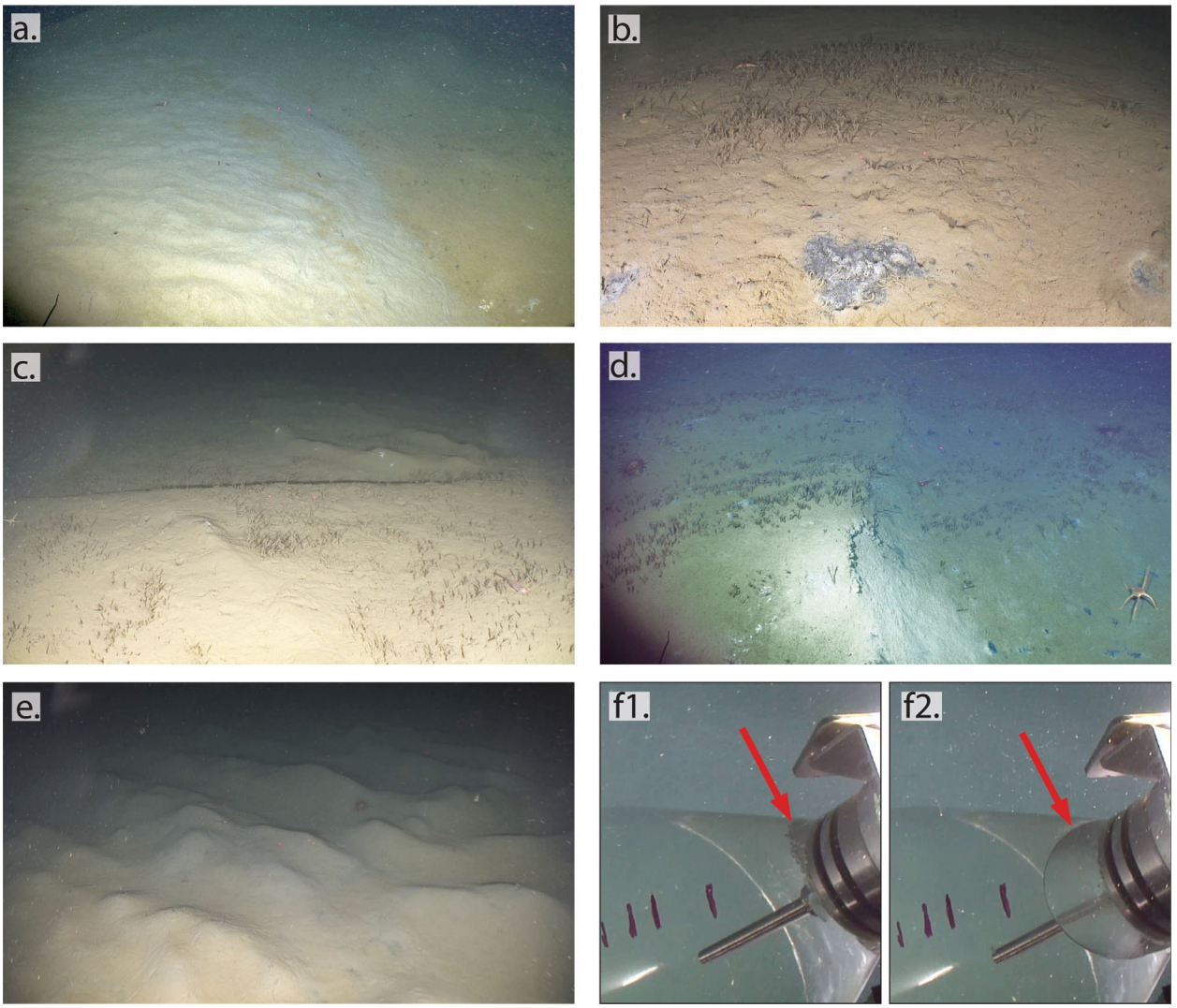

Figure 6. Video images showing the top of the mud volcanoes. (a) Area interpreted to be the edge of a young flow devoid of sessile organisms (lighter colored and slightly elevated area to the left), and darker area to the right colonized with tubeworms. (b) Patch of black sediment rimmed with white mat and very small worms in the surrounding area. (c) Ridge truncations and worm patches. (d) Small scarp (~15 cm high) that offsets a tubeworm-bearing ridge and exposes fresher appearing tubeworm-free face. (e) Hummocky bottom in an area devoid of sessile organisms. (f1 and f2) Gas sampling. (f1) Before the heater is turned on, the bubbles captured within the funnel form a mush of gas hydrate-coated bubbles indicated by red arrow. (f2) After the heater is turned on, the hydrate decomposes and leaves a distinct gas headspace indicated by red arrow.

3.2. Seafloor ROV Observations

Visual observations were made during ROV transects across the flanks and plateaus of the circular structures at the three sites, including the conical mound at the ~740 m feature (Figures 2b–2d) (http://www.mbari.org/arctic_shelf_edge/). Two distinct types of surface textures were seen on the surface of these plateaus. One consists of light gray areas commonly tens of meters across and conspicuously devoid of sessile organisms (i.e., worm tubes and mats) and sometimes even noticeably lacking in mobile megafauna (Figure 6a). These areas are slightly elevated (i.e., 5–20 cm) with respect to the other observed surface texture, which is olive or tan colored and is characterized by the presence of colonies of small worm tubes sticking up to ~5 cm out of the seafloor (Figures 6b–6d). The size of these colonies range from isolated clusters ~10 cm across with only a few dozen individuals, to extensive thickets of worms filling most of the field of view of the ROV camera (i.e., ~3 m). Black substrate is exposed around burrows, within depressions (Figure 6b) and where the ROV disturbed the surface sediments. Some burrows are rimmed with white halos, presumably associated with bacterial mats (Figure 6b). In places sharp boundaries between the two textures were seen. However, some areas appear to be transitional between the two bottom types.

Except for the smooth surface of the large conical feature at 749 m, a distinct fine-scale morphology composed of small ridges, scarps, and hummocky bottom (Figures 6c and 6d) was observed on the surfaces of the flat-topped plateaus at the three sites. The slightly arcuate ridges are up to 50 cm high and 1–2 m across, sometimes occurring in concentric sets 1–5 m apart. In places the ridges change direction abruptly as they terminate against another set of ridges (Figure 6c). Fresher appearing sediment is visible on scarps of 20 cm–1 m in height (Figure 6d). Patches of hummocky bottom, possibly indicating rapid dewatering of high water content sediments, are common, irrespective of the degree of worm colonization (Figures 6a and 6e.)

The seafloor on the surface of all three flat-topped circular plateaus is similar and no distinctions could be made between them based on the ROV observations. However, the large conical mound at the ~740 m feature (Figure 7) was distinguished by its smooth surface (e.g., lacking small ridges or scarps) and by being almost entirely devoid of sessile organisms.

Gas bubbles were seen emanating from several 0.5 to 2 cm in diameter holes or burrows in an area covered with thick worm clusters on the surface of the plateau in 420 m water depth during a ROV dive in 2012 (http://www.mbari.org/arctic_shelf_edge/). Bubbling occurred at variable rates and shifted between nearby holes. Bursts of bubbles emanated from several individual holes that slowed before ceasing over a few minutes. When captured by the overturned funnel mounted on the ROV, bubbles became coated with gas hydrate (Figure 6f1), which converted back to gas once the heater inside the funnel was turned on. The gas was then withdrawn into a preevacuated cylinder (Figure 6f2).

3.3. Faunal Composition and COI Mitochondrial DNA of Tubeworms

Genetic analyses of the six tiny tubeworms collected with the ROV on the circular plateau at 420 m water depth (Figures 3c, 3d, and 6b–6d) indicated that all were the same species and their COI mitochondrial DNA sequences [*Vrijenhoek et al.*, 2009] were about ~97% similar to those of siboglinid tubeworms (*Oligobrachia haakonmosbiensis*) identified from the Haakon Mosby mud volcano [*Lösekann et al.*, 2008]. A tissue sample of a siboglinid tubeworm yielded a δ^{13}C value of $-55.0‰$ PDB and contained $31.6 \pm 0.2\%$ modern carbon.

ROV video observations show high abundances of the tiny *Oligobrachia* sp. (i.e., *Siboglinidae polychaete* tubeworms) on the surfaces of the circular plateaus at the three sites. Bacterial mats are common and comparatively high abundances of shrimp (both Caridea and Mysida) and fish (including Agonidae, Cottidae, Hexagrammidae, Lophiiformes, Pleuronectiformes, Rajiformes, *Sebastes* sp., and Zoarcidae) were noted on these features compared to other dives on the slope.

3.4. AUV Surveys

The AUV surveys have enabled accurate rendering of the seafloor morphology and subbottom characteristics of the circular features and their surroundings. When compared with conventional hull mounted multibeam and pingers, the resolution of the AUV data is significantly enhanced because it is operated near the seafloor. For example, during operations at 50 m above bottom, the footprint at nadir for a 1° by 1° multibeam sonar is 0.87 m, enabling 1 m data gridding. In comparison, similar sonar operated from a surface vessel in 740 m water depths has a beam footprint of 12.9 m.

3.4.1. The 740 m Feature

The characteristically 0.8°–1.0° seafloor slope is interrupted at ~750 m water depth by a distinct 3 km wide arcuate scarp (Figure 2d). The headwall scarp on the southern (upslope) flank is ~30 m high with an average slope of $\geq$5°. Three elevated circular structures with diameters of up to 630 m are enclosed within the 3 km wide arcuate scarp (Figures 2d, 7a, 7b, and 7f). Two of these features stand at or above the level of the surrounding seafloor. Although less obvious, scarps with $\leq$1 m relief can be traced downslope, showing the 3 km wide scarp is a part of a 3 km in diameter circular structure with a down-dropped center (Figures 2d, 7a, 7f, and 8).

The most prominent of the enclosed circular features is a nearly flat-topped plateau that stands ~30 m above the floor of the arcuate scarp (Figure 2d). Depth on the top of this plateau only varies from 741 to 745 m, except for one subtle cone on the southern rim, which shoals to 737 m water depth (Figures 2d and 7).

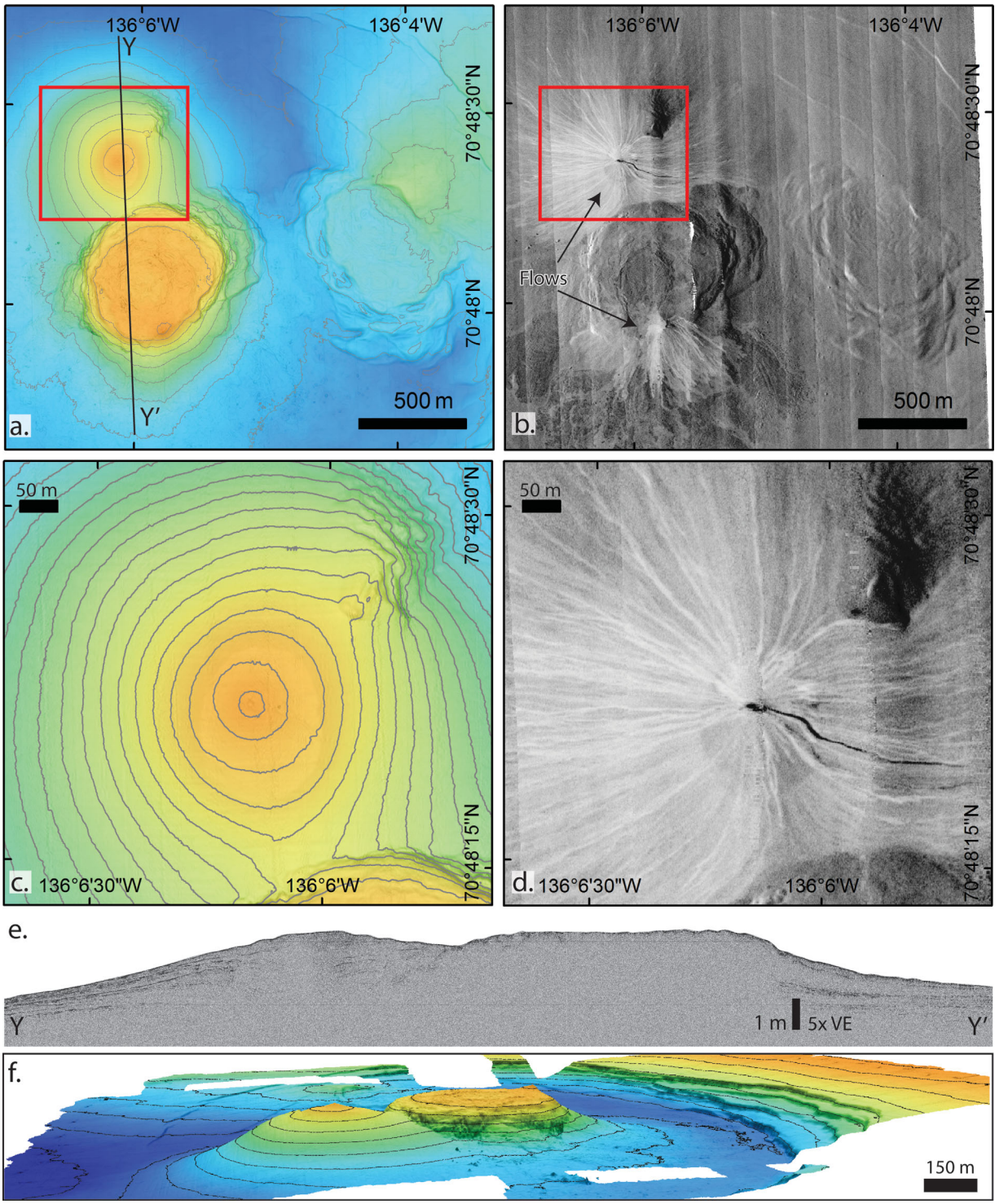

Figure 7. (a and c) The detailed morphology of a cluster of three mud volcanoes in ~740 m water depth is illustrated with AUV collected high-resolution bathymetry, (b and d) side scan backscatter intensity, (e) chirp subbottom profile, and (f) a perspective view. Figure 7a shows one nearly flat-topped, one nearly conical, and a partly collapsed ovoid-shaped feature to the east (color-scale depths from 786 to 721 m and 5 m contour intervals). Black line indicates location of chirp profile Y-Y′ in Figure 7e. The intensity of side scan data is displayed on a relative scale with darker shades indicating stronger reflections. Figure 7b is side scan backscatter of same area as in Figure 7a. Area covered in more detail in Figures 7c and 7d is indicated with red boxes in Figures 7a and 7b. Figure 7c shows bathymetry of conical mud volcano with 2 m contours (color-scale depths from 777 to 721 m). Figure 7d shows side scan data of the surface of conical mud volcano showing numerous trails of relatively low backscatter emanating radially from the crest of the feature. Figure 7e shows an increased separation between subbottom reflectors under the flanks in proximity to the mud volcano, which indicates these flanks are formed by sediments delivered by the mud volcano. Figure 7f shows the same site from an azimuth and elevation of 104° and 7°, respectively, color-scale depths from 790 to 720 m, with 5 m contours and a 5X vertical exaggeration.

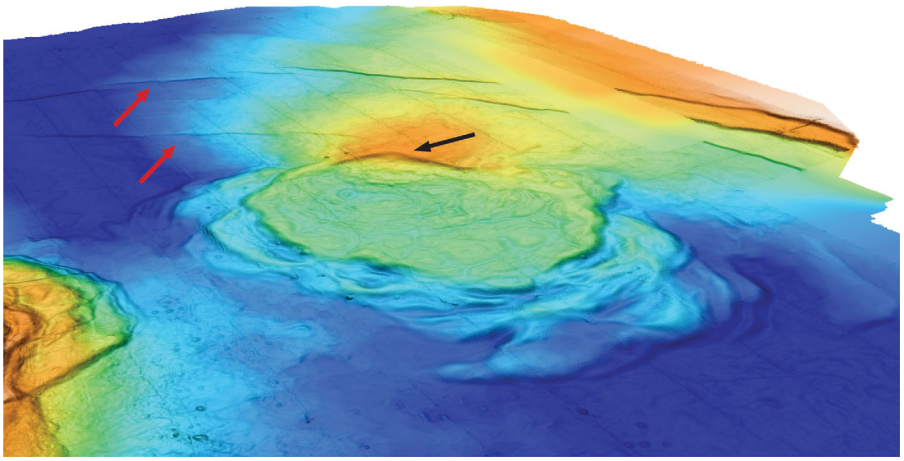

Figure 8. Perspective view of the ovoid-shaped feature at ~740 m water depth from an azimuth and elevation of 36° and 30°, respectively. Color scale extends between 782 and 755 m. No vertical exaggeration. Black arrow shows location of scarp and fan of sediment flows that are now elevated with respect to the level of the ovoid flat-topped plateau. Subtle scarps which form the northern side of the 3 km in diameter circular structure is indicated with red arrows.

The plateau has a slightly depressed center (~741 m water depth), is rimmed by a higher edge, and its flanks slope at up to 13° toward the floor of the arcuate scarp.

To the north, there is a smooth-textured conically shaped feature with a well-defined top at 741 m water depth, standing ≤28 m above the floor of the arcuate scarp (Figure 7c). The sides of this feature consistently slope at 4.1° ± 0.1°. The southern slope merges with the northern flank of the circular plateau to the south.

The third elevated feature, to the east of the other two, is ovoid in shape, ~600 by ~330 m across, with a nearly flat central plateau (771.5 ± 1.0 m) rimmed by a subtly elevated ridge (Figures 2d, 7a, and 7b). This plateau is surrounded by complicated morphologies not seen around the other two features in this cluster. Half of the plateau is surrounded to the south and west by a series of arcuate ridges and troughs with 4 m of relief at a lower elevation than the plateau (Figures 7a and 8). These ridges are of a similar size to the rim of the nearly level plateau. Northeast of the ovoid plateau a truncated fan gently slopes to the NE forming an arcuate scarp that rises ~11.5 m above the ovoid plateau. The fan apron appears to cover the arcuate scarp that otherwise rims the 3 km in diameter circular feature (Figures 2d and 8).

Side scan backscatter (Figures 7b and 7d) from these features show areas of distinctively stronger (darker) and weaker (lighter) backscatter intensity that are in sharp contrast to the medium uniform backscatter of the background slope. Trails of weaker backscatter, 2–5 m wide and up to 600 m long, radiate in all directions from the crest of the cone-shaped feature (Figures 2d, 7b, and 7d). Similar weaker backscatter trails, ~5 m wide and up to 350 m long, radiate downslope from the top of the small cone on the southern rim of the large flat plateau, and create a fan pattern that ends where the dip of the basin within the arcuate scarp reverses (Figures 2d and 7b). In contrast, a ~3 m wide trail of distinctly stronger backscatter, connected to a ~7 m wide equally strong backscatter patch atop the main conical feature, extends for 300 m downslope to the east south east across its flank (Figures 7b and 7d). Although both the single trail of relatively high backscatter and the numerous trails of relatively low backscatter are obvious in the side scan, these acoustic signals are not associated with identifiable morphological expressions in the bathymetry (e.g., ~25 cm).

3.4.2. The 420 m Feature

The otherwise smooth bathymetry of the Beaufort Slope is interrupted at ~400 m water depth by an elevated, flat-topped, approximately circular plateau, 1100 m in diameter (Figures 2a, 2c, and 9). A distinct ramp, 50–100 m wide dipping 12° over 5–15 m of relief, forms the flanks of the plateau. There is no indication that the relief is attributable to slope failures that removed the surrounding host sediments. While a subtle warping in the regional bathymetric contours occurs out to more than 500 m from the ramp, the surrounding area has a slope that is similar to the regional gradient (i.e., ≤1°).

Fine-scale morphologies with ≤2 m of total depth variation (i.e., between 418 and 420 m) are clearly seen atop the plateau in the AUV-generated bathymetry (Figure 9c). These textures consist of

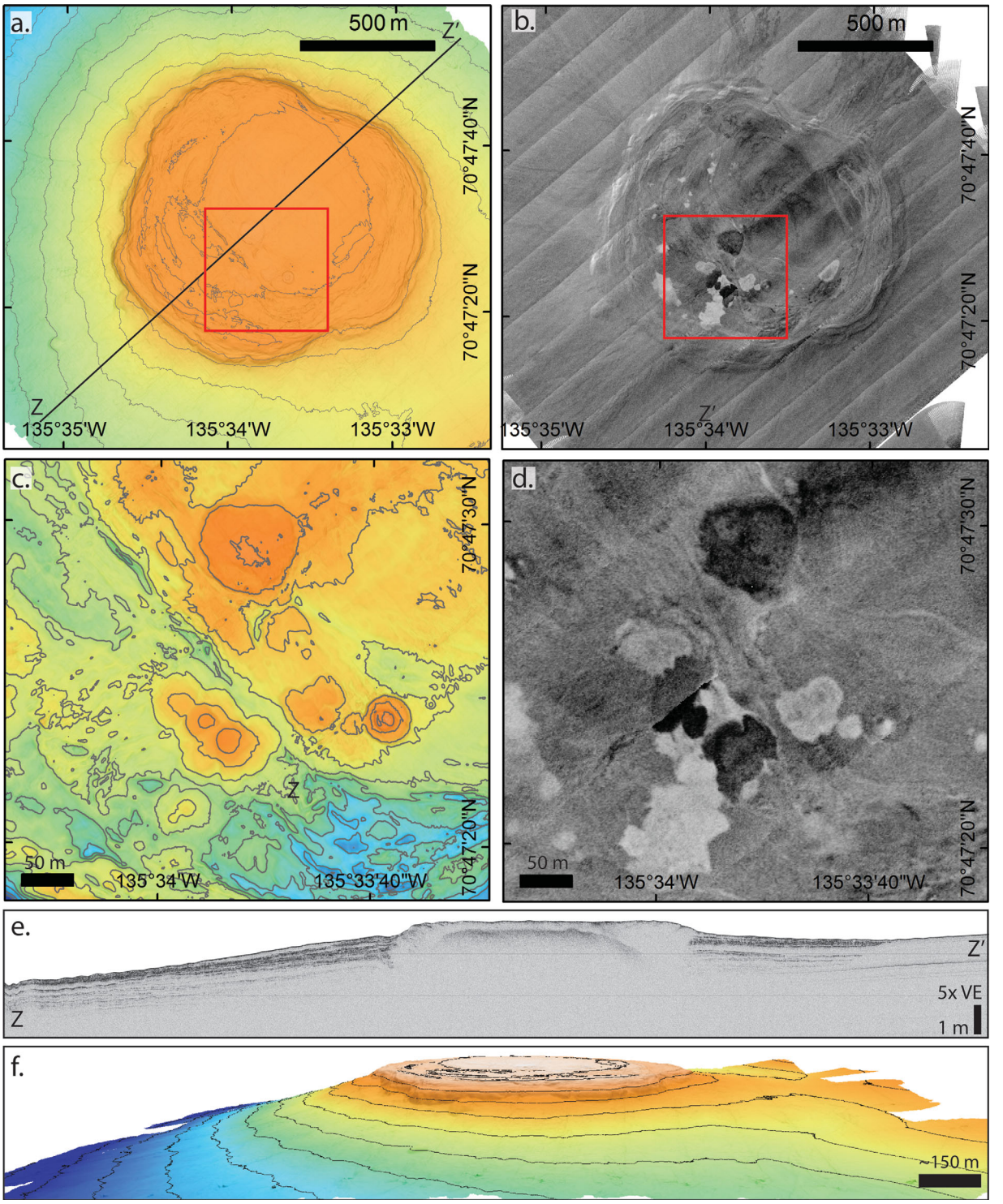

Figure 9. (a and c) The detailed morphology of the ~420 m mud volcano is illustrated with AUV collected high-resolution bathymetry, (b and d) side scan backscatter intensity, (e) chirp subbottom profile, and (f) a perspective view. Figure 9a shows one flat-topped elevated feature with color-scale depths from 460 to 412 m (contour interval of 5 m). Black line indicates location of chirp profile Z-Z′ in Figure 9e crossing ~NE-SW over crest of flat-topped plateau. The intensity of side scan backscatter data is displayed on a relative scale with darker shades indicating stronger backscatter. Figure 9b shows side scan backscatter of same area as in Figure 9a. Area covered in more detail in Figures 9c and 9d indicated with red box in Figures 9a and 9b. Figure 9c shows bathymetry of area on the surface of plateau with 50 cm contour lines and entire depth range in color scale of 423–417 m. Figure 9d shows side scan backscatter of same area as Figure 9c. Figure 9e shows the increased separation between subbottom reflectors under the flanks in proximity to the mud volcano, which indicates these flanks are formed by sediments delivered by the mud volcano. Figure 9f shows the same site from an azimuth and elevation of 41° and 8°, respectively, color-scale depths from 470 to 418, with 5 m contours and a 5X vertical exaggeration.

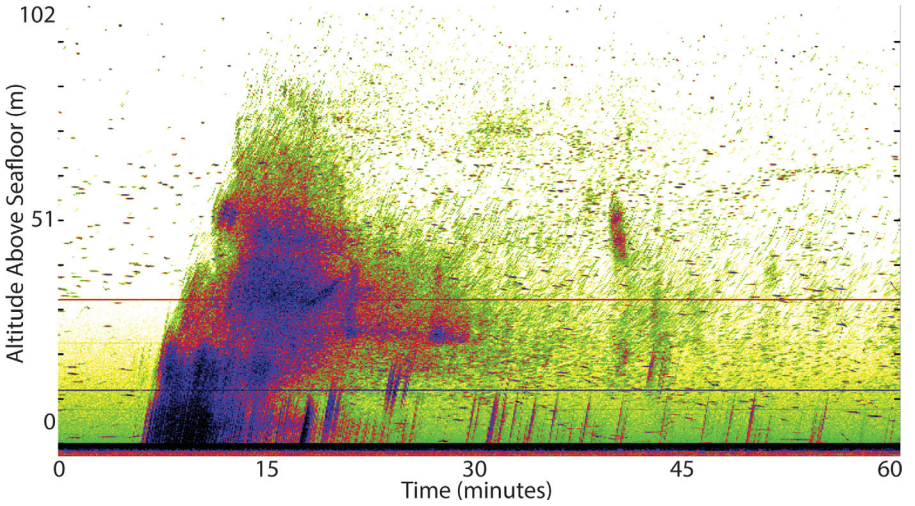

Figure 10. Echoes detected by down-looking sonar suspended 110 m above the ~282 m mud volcano; signals have been corrected for transmission loss; dark horizontal lines are echoes from floats on the mooring. The intense feature beginning about 7 min into the record reflects a rapid release of many bubbles from the seabed directly beneath the sonar; these rise to more than 80 m elevation during the next 10 min. This intense event waned after about 15 min, to be supplanted by a more typical pattern—quasiperiodic events. Echoes appearing higher in the water column are from bubbles released elsewhere on the feature that have drifted into the beam.

approximately circular flat-topped mounds 10 m to more than 75 m in diameter typically with 0.1–1 m relief (Figure 9).

Side scan backscatter on the ~420 m feature also shows distinctive patches of stronger and weaker backscatter intensity. There is a degree of correspondence between the location of distinctive backscatter patches atop the plateau and the location of bathymetric highs (Figures 9c and 9d). These topographic highs display either high or lower backscatter, which contrasts with the intermediate backscatter intensity of the generally homogeneous background areas (Figure 9d). Concentric rings of slightly lower backscatter than the slope at large are discernible surrounding the plateau (Figure 9b).

3.5. The 282 m Feature

Surface ship multibeam bathymetry revealed a circular feature ~660 m in diameter at 282–286 m water depths on the slope (Figure 2b). The feature is subtle as it is primarily distinguished as a nearly flat area delineated by an outer trough that is ~50–100 m wide and 1–3 m deeper than the surrounding seafloor, which slopes at 0.8°–1°. The downslope side of the ~282 m feature is elevated a few meters above the surrounding seafloor.

3.6. Ground-Truthing AUV Surveys With ROV Dive Observations

Most of the ROV dives occurred in 2012 before the AUV surveys were conducted. However, subsequent comparisons show that the widespread areas of intermediate intensity backscatter seen in the side scan are commonly associated with siboglinid tubeworms communities (http://www.mbari.org/arctic_shelf_edge/).

In 2012, ROV Dive 6 crossed the trails of high and low-intensity backscatter seen in the side scan at the conical mound in ~740 m water depth (Figures 2d and 7d) and surveyed the top of the mound where they appear to originate. No sessile organisms were seen at the top of this conical mound. Curiously, no obvious visual distinctions could be made between areas of lower-intensity backscatter on the flanks of the conical feature and the distinctively higher backscatter on its crest.

In 2013, ROV Dive 24 was focused on investigating the seafloor textures of the distinctive, higher backscatter and elevated circular features on the ~420 m feature and the lobes of low backscatter nearby. Unfortunately, the total navigational errors (≥50 m) were too large to confidently match locations between the AUV and ROV surveys. However, widespread areas that are notably devoid of sessile organisms were found

on this dive. Again, no observations that help explain the distinction between the areas of the seafloor associated with the strongest and weakest backscatter were made on this ROV dive either.

3.7. Seafloor Observations From Mooring

A yearlong record of temperature and conductivity 5 m above the seabed over the ~282 m feature shows a mean annual temperature of 0.282 ± 0.266°C with variations in temperature ranging from -1.12 to $+0.55$°C with corresponding salinity from 33.85 to 34.85 ppt at a pressure of 278 ± 0.5 dB. The stability of methane hydrate was evaluated (see section 4.4) based on the measured gas composition (Table 1), temperature and salinities at 5 m above the seafloor at the shallowest mud volcano (~282 m water depth) using the Colorado School of Mines CSMgem gas hydrate phase program [*Sloan and Koh*, 2008].

The down-looking sonar recorded water column echoes at intervals throughout the 12 months of operation. The majority of these echoes are consistent with backscatter from rising gas bubbles (or gas hydrate-coated bubbles) released at the seabed directly at or relatively close to the site of the mooring. The gas release events varied in character and periodicity (Figure 10). The most common signatures are the quasi-periodic slanted lines of backscatter on the elevation-versus-time plot, which originate at the seabed. More energetic events were also observed, including that displayed in Figure 10.

Sound recordings were also consistent with intermittent releases of small groups of bubbles. However, detections of bubbles via ambient sound were much less frequent than those by sonar.

4. Discussion

4.1. Mud Volcano Morphology

These detailed investigations confirmed that the circular topographic features found at the three sites are mud volcanoes formed due to sediment accretion by episodic discharges of mobile sediment [i.e., *Milkov*, 2000; *Dimitrov*, 2002; *Kopf*, 2002]. All of them are elevated with respect to the surrounding seafloor. Reflectors in the chirp data and sediment cores show that the flanks of the mounds are composed of wedges of sediment that thicken toward the elevated topography (Figures 2e, 2f, 7e, and 9e) demonstrating that they are constructional aprons formed by discrete sediment flows delivered from the adjacent topographic high.

Recent flows on the features themselves are identified in side scan data as distinctive trails of varying backscatter intensity (Figures 7b, 7d, 9b, and 9d). At the ~740 m mud volcanoes, these flows form long-thin trails of either high or low backscatter running down the $>4°$ slopes of the flanks. At the ~420 m mud volcano, recent flows are outlined in the side scan data as circular congealing mud ponds. At both sites, the surfaces of recent flows are devoid of sessile organisms.

The multiple, low-relief (i.e., 0.1–2.0 m high), circular features on the plateau at ~420 m water depth (Figure 9) indicate numerous venting sites and suggest that the location of the vents has shifted. Some flows apparently filled subtle depressions forming gravity-leveled sediment ponds textured by subtle circular mud boils and concentric ridges on the surface of the congealing mud ponds. While the extreme vertical exaggerations seen in Figures 2e, 2f, 7e, 7f, 9e, and 9f make these features appear steep, their tops are nearly flat. This suggests that the flows have a low viscosity and are only contained by a stiffer rim, which is occasionally overtopped. Flow emanating from the tops of these plateaus will fill any depressions found on them.

The existence of subtle depressions in the interior of the plateaus of the mud volcanoes at the ~420 and ~740 m water depths suggests that the surface experiences subsidence, perhaps due to deflation of underlying chambers or dewatering and collapse of older flows. This subsidence leaves slightly elevated rims on the edges of the plateaus. Subsequent flows cover earlier flows and refill depressions that have developed, while acting to keep the tops of the plateaus essentially level.

The surface morphology consists of elements produced by the eruption of fluidized material. Small scarps and intersecting ridges on the surfaces of the plateaus (Figures 7d and 7e) suggest that vertical and perhaps horizontal movements occur on the surface. These scarps may be created by relative surface displacements due to compaction of previous flows or horizontal motion of a surface crust on the plateau. Similar surface features have been seen on other marine mud volcanoes where both lateral and vertical movements in the surface layers have been documented by both repeat mapping and movements recorded in deployed

equipment [*Feseker et al*., 2008, 2014; *Foucher et al*., 2010]. The truncated fan and scarp above the ovoid feature at the ~740 m mud volcano (Figure 8) shows that venting has occurred ≥11.5 m higher than the present level of the ovoid plateau. This suggests extensive deflation of the area under the ovoid plateau since the last major eruption(s).

4.2. Venting Fluids, Gas, and Sediment

The ROV observations of gas bubbles escaping from the top of these mud volcanoes (Figure 6f), the vigorous release of methane upon core recovery, and the moussey textures in the cores collected from these morphological features (Figure 3a) confirm that the interstitial gas concentrations are at or near saturation close to the seafloor [*Paull and Ussler*, 2001]. The escaping gas is largely methane and its isotopic composition ($\delta^{13}C \sim -64‰$ (PDB) and $\delta D \sim -222‰$ (SMOW)) shows it is primarily of a biogenic origin [e.g., *Whiticar*, 1994]. The initial observations made from the 200 kHz downward looking sonar indicates that episodic eruptions of gas occurred during the 2012–2013 mooring deployment. As shown in Figure 10, the nature of gas release can vary substantially with large events occurring over a prolonged period and minor events occurring repetitively over short periods.

The extrusion of fluidized material on mud volcanoes requires that overpressure conditions exist in the subsurface [*Dimitrov*, 2002; *Kopf*, 2002]. Expansion and resulting pore pressure increase associated with rising gaseous methane is inferred to reduce the shear stress of the affected sediments causing fluidized/gasified sediment eruptions. These sediment discharges then move downslope and accumulate as ramparts. The sharp decrease with depth in pore water chloride and sulfate concentrations and the rapid increase in sediment temperature near the seafloor imply low-chloride, sulfate-depleted, warm fluids are escaping from these structures, in addition to methane.

Evidence as to the source of the fluids that are being expelled from these mud volcanoes is provided by the elemental and isotopic compositions of the pore water. Their most salient characteristics are unusual low chloride concentrations, negative $\delta^{18}O$ and δD values, and major element concentrations that depart from the constant composition ratios of seawater (Figures 4c and 4d and Table 2). Moreover, pore waters isotopic compositions plot to the right of the seawater-meteoric water mixing line, as approximated by the projection of the local meteoric water line (Figure 5a).

Both gas hydrate formation and meteoric water sources can decrease $\delta^{18}O$ and δD values of pore waters of marine sediments [*Tomaru et al*., 2006]. Gas hydrate formation, however, can be precluded, as it would increase the pore water salinity while maintaining the ratios of dissolved constituents unchanged. Moreover, the near-seafloor high thermal gradients prevent gas hydrate formation at depth.

A mixture of meteoric water and seawater would produce negative $\delta^{18}O$ values, negative δD values and low chloride concentrations. The existence of meteoric waters on sediments of the slope of the Beaufort Sea is consistent with the gradients in chloride observed in pore water sampled in the background piston cores (Figure 4a). The $\delta^{18}0$ values of $-19.7‰$ to $-22.4‰$ of the freshwater component in pore waters from the slope were identified by extrapolation to zero chloride (Figure 5b), which match with modern precipitation and groundwater recharge at the latitude of the Beaufort Sea coastal areas (Figures 4c and 4d) [*Michel*, 1986; *Mackay and Dallimore*, 1992; *Moorman et al*., 1996; *Michel*, 2011; *Lacelle*, 2011].

The occurrence of brackish pore waters at the shelf edge and slope of the Beaufort Sea has independently been measured and inferred from models that are associated with the decomposition of permafrost and regional hydraulic gradients [*Paull et al*., 2011; *Pohlman et al*., 2011; *Taylor et al*., 2013; *Frederick and Buffett*, 2015]. However, a simple mixture of meteoric water and seawater would have an isotopic composition along the local meteoric water line and would not explain the altered elemental composition ratios with respect to seawater observed in pore waters of the mud volcanoes.

A substantial body of literature exists on the impact of subsurface processes in the evolution of pore waters emanating from mud volcanoes. These studies show substantial alterations of pore waters chemistry which is attributed to clay dehydration during smectite to illite transition [e.g., *Dia et al*., 1999; *Brown et al*., 2001; *Dählmann and de Lange*, 2003; *Godon et al*., 2004; *Hensen et al*., 2004; *You et al*., 2004; *Mazzini et al*., 2007, 2009; *Chao et al*., 2013; *Li et al*., 2014]. Clay dehydration produces water with positive $\delta^{18}O$, negative δD values, and rich in sodium.

The waters emerging from the three mud volcanoes are the net result of the combination of three water end-members. The background cores show pore waters are comprised of a mixture of seawater and Arctic meteoric water. Prior to emerging from the mud volcanoes waters produced in clay dehydration are added to this mixture. The resulting waters have negative δ^{18}O and δD values and are rich in sodium relative to other ions compared to seawater ion ratios. Calcium and magnesium concentrations may be affected by authigenic carbonate precipitation, as inferred by the high alkalinity. Because the chemistry of the waters that are being expelled at the ~282, ~420, and ~740 m mud volcanoes differ (Figures 4c and 5a and Table 2), these waters reflect different sources at depth and/or varying extent of mixing along their transport pathway before emerging to the seafloor.

The composition of these fluids provides some constraint on the minimum depth of their source as the smectite to illite transition is affected by temperature, pressure, time, and composition, but the conditions of its onset are not precisely known [e.g., *Hoffman and Hower*, 1979; *Buatier et al*., 1992; *Velde and Vasseur*, 1992]. Laboratory and modeling studies do not start at temperatures of less than 20°C [*Lawrence et al*., 1975; *Buatier et al*., 1992; *Sheppard and Gilg*, 1996]. Minimum temperatures of ~60°C have been inferred in several studies [e.g., *Jennings and Thompson*, 1986; *Freed and Peacor*, 1989; *Kastner et al*., 1993; *Velde and Vasseur*, 1992] and clearly continue until over 200°C [i.e., *Jennings and Thompson*, 1986]. Given a maximum geothermal gradient of 0.08°C per meter measured from permafrost-free areas of the Beaufort Slope [*Riedel et al*., 2014; *Jin et al*., 2015], the 60°C isotherm is estimated to be at ≥750 m below the seafloor. Studies of the smectite to illite transformation in >3 km deep exploration wells under the adjacent Beaufort continental shelf, where permafrost occurs up to ~600–700 m below the seafloor [*Taylor et al*., 2013], suggest that the onset of smectite to illite transformation occurs at ~1.5–2.0 km subbottom depths, where the temperatures have reached 50°C and overpressured conditions exist [*Ko*, 1992; *Ko and Hesse*, 1998]. Furthermore, the absence of higher hydrocarbon gases and oil suggests that the source for the methane driving the sediment expulsion is also shallower than the window (>150°C) for thermogenic hydrocarbon generation [*Quigley and Mackenzie*, 1988; *Hunt*, 1996]. It is noted that the source depth of the extruded solids may be different from the source depth of the water and gas that are expelled on mud volcanoes [*Haeckel et al*., 2007; *Reitz et al*., 2011].

4.3. Chemosynthetic Communities

The presence of methane in proximity to the seafloor at these sites suggests that the extensive thickets of siboglinid tubeworms and white bacterial mats are part of a chemosynthetic ecosystem (Figures 3c, 3d, and 6b–6d). The closest known relatives to the siboglinid worms sampled from the top of the ~420 m mud volcano (*Oligobrachia haakonmosbiensis*) come from a similar environment at the Håkon Mosby mud volcano, which is at the gateway to the Arctic Ocean Basin [*de Beer et al*., 2006]. *O. haakonmosbiensis* is also known to host methane and/or sulfide-oxidizing bacteria. This interpretation is further supported by the δ^{13}C content (−55.0‰ PDB) of their tissue carbon, which is ~28.4‰ more depleted than the organic carbon (−26.4 ± 0.6‰ PDB) found in the surrounding sediments. This value is atypical of organisms that are solely supported by photosynthetic ecosystems, and more consistent with a highly depleted ^{13}C carbon source such as methane [*Paull et al*., 1985]. Where the sulfate from the overlying seawater is mixed with the escaping methane-bearing pore fluids near the seafloor, anaerobic methane oxidation produces sulfide, which supports microbial primary production [e.g., *Boetius et al*., 2000]. The siboglinid worms, which were alive when sampled, only had 31.6 ± 0.2% modern carbon, which indicates the majority of the carbon in their tissue and tube was assimilated from ^{14}C-depleted methane [*Paull et al*., 1989].

These are the first documented chemosynthetic biological communities on the flanks of the western Arctic Ocean. This site appears to have a fauna that is similar to that found on the Håkon Mosby mud volcano in the Norwegian Arctic [*Lösekann et al*., 2008].

The biological communities on these mud volcanoes and on the Håkon Mosby mud volcano are notable in their absence of clams (i.e., Vesicomyidae), mussels and larger Vestimetiferan tubeworms that characterize many similar methane-bearing seep sites elsewhere in the world [e.g., *Sibuet and Olu*, 1998; *Olu-Le Roy et al*., 2004; *Werne et al*., 2004]. Also notably absent were visible accumulations of methane-derived authigenic carbonates which are commonly exposed on the seafloor around methane seepage sites elsewhere, including the surface of some mud volcanoes [e.g., *Lance et al*., 1998]. Such phenomena create distinctive seafloor morphologies easily identifiable in AUV survey data [e.g., *Paull et al*., 2015]. The observed high alkalinity and

depletions in pore waters calcium and magnesium (Figure 4c) is consistent with authigenic carbonate formation. However, the megafaunal communities and authigenic carbonates typical of methane seep sites form slowly [i.e., *Olu-Le Roy et al*., 2004]. One explanation for the lack of these common seep indicators is that the tops of these structures are too active for accumulations of slow forming megafaunal communities and for observable accumulations of methane-derived authigenic carbonate.

4.4. Gas Hydrate Stability Conditions

At the temperature, pressure, and salinity conditions measured 5 m above the seafloor over the ~282 m mud volcano, conditions appropriate for methane hydrate stability persisted for the entire 1 year mooring deployment given dissolved methane concentrations ≥0.1% molar fraction (CSMgem) [*Sloan and Koh*, 2008] and seawater CO_2 concentrations. Thus, the top of the methane hydrate stability field was in the water column at depths <282 m and the base of the methane hydrate stability field was in the sediments at all these mud volcanoes.

ROV observations show that hydrate skin forms quickly on the surface of escaping methane bubbles from the ~420 m mud volcano [e.g., *Brewer et al*., 1997; *Sauter et al*., 2006]. The presence of gas hydrate near the seafloor was confirmed in cores from the ~740 and ~420 m mud volcanoes. However, the rapid increase in temperature with subbottom depth (commonly 2.2°C per m) [*Riedel et al*., 2014] restricts the methane hydrate stability zone to a thin near-seafloor zone on the crest of these features. The methane hydrate stability zone may only be a few cm thick at the ~282 m mud volcano and a few meters thick on the ~740 m mud volcanoes.

During eruptions, methane bubbles may form by exsolution within the fluidized sediment column because the solubility of methane decreases with the decreased pressure in the ascending material [*Sloan and Koh*, 2008; *Paull et al*., 2011]. As the eruptions occur, gaseous methane will be released into the water column as eruptive bursts (Figure 10). Bubbles also escape as smaller quasiperiodic events that may only involve a few bubbles at a time (Figures 6f and 10) (http://www.mbari.org/arctic_shelf_edge/).

During eruptions some methane bubbles will inevitably also remain trapped within the extruded flows and, as the flows cool on the seafloor, stable methane hydrate will form quickly. Thus, fresh flows may lock in gas hydrate-coated bubbles. However, gas hydrate trapped within the flows will come into contact with the distinctly methane-undersaturated seawater and experience relatively rapid dissolution [*Lapham et al*., 2014], probably disappearing from the upper few cm before the mud has extensively congealed.

The methane hydrate phase stability zone extends into the water column above all these mud volcanoes. While its upper limit level is expected to be seasonally variable, the top of the gas hydrate stability zone may extend to ~250 m water depths at times, which is shallower than typical for most continental margins [*Sloan and Koh*, 2008]. This unusually shallow depth for methane hydrate stability is a consequence of the cold-water mass covering the upper continental slope of the Beaufort Sea [*McLaughlin et al*., 2004].

4.5. Controls on Vent Elevation and Seafloor Morphology

The common elevations of the flat-topped plateau and the conical structure at the ~740 m mud volcano (Figure 7) versus the distinctly deeper elevation of the top of the ovoid feature (~772 m) are intriguing. Conceptually, for an active mud volcano, we envisage that the height of a feature is related to the magnitude of the subsurface overpressure and the resistance of the shallow sediments that are upwardly deformed or breached by a fluid breakthrough. As the cover sediments at all three sites is likely quite similar, the varying height of the features may suggest some variability in the subsurface overpressure at the fluid source. For instance, the common elevation of these features may suggest a common source whereas the deeper feature may have a somewhat different source with lower overpressure. Alternatively, the height of the feature may simply indicate the relative age of the features, where the cone is the youngest and the plateaus are formed by continuing eruptions, which consistently rise to the same level, progressively forming the nearly flat-topped plateaus.

Evidence for surface subsidence in the ovoid mud volcano can be found in the morphological elements surrounding the terrace. The presence of a fan extending NE from the rim of the ovoid terrace suggests that flows once ran downslope (NE) away from what is now the central ovoid plateau (Figure 8). However, this would require that the level of the central sediment pond was higher in the past but has deflated because the beginning of the flow trails that once emanated from its interior stand higher than the present level

of the sediment pond. The collapse of the surface of this feature may explain the formation of the scarp on the NE side of the pond and of the high ridges that rim most of its flanks. The similarity of the rim around the present plateau with the outer lower ridges that partly surround this structure suggests that these might have been the rims of earlier plateaus (Figure 8).

When fluidized sediment ascends to the seafloor, gas will escape as the sediment flow spreads out onto the seafloor. The viscosity of the sediment will progressively increase as degassing continues, ultimately resulting in sediment consolidating. The slope of the seafloor accreted from these flows appears to reflect these changes in viscosity, with only slight or nonexistence slopes developed on the crest of the plateaus where the lowest viscosity flows may occur. Conversely, the steep flanks (~13°) on the outer rims of the flat-topped plateaus indicate that once sediment flows reached the edges of the plateau they have degassed enough to gain considerable viscosity and dribble down the outside rim to produce the sharp slopes.

4.6. Morphological and Biological Succession

The ROV dives showed a fine-scale topography consisting of rings of concentric ridges, small scarps that appear to offset a surface crust, hummocky topography, and variations from areas distinctly devoid of sessile organisms to those heavily colonized. These patterns appear to be manifestations of both morphological and biological successions.

The areas on the seafloor with distinctively higher and lower backscatter are interpreted to be associated with relatively young events, compared to the more extensive background areas of intermediate backscatter. The top of the conical feature at the ~740 m mud volcano is interpreted to be the source of numerous flows, identified by the backscatter trails (Figure 7d). While most of these trails have lower backscatter, the crest of the mud volcano is associated with a high backscatter cap that connects to a single high backscatter flow. Because this high backscatter cap and flow overlie many other flows, it is inferred to be associated with the most recent flow event. By inference, the most recent flows on the crest of the ~420 m plateau can also be identified as high backscatter areas (Figures 9b and 9d).

Significantly, during ROV dives visual observations failed to detect differences between the areas with the highest and lowest backscatter in the AUV surveys (Figures 7 and 9). One explanation is that sediment flows too young to be fully degassed are gas bubble charged or gas hydrate bearing, which results in high backscatter and makes them easily discriminated in the side scan data. Once the methane hydrate and bubbles trapped near the seafloor have dissolved, the backscatter intensity decreases, yet in both cases flows are too young to be substantially colonized, and the sediment is barren. Therefore, no visual distinction is possible between the areas with the lowest and highest backscatter intensity. Relatively low backscatter intensity has also been noticed on the surface of mud volcanoes off Barbados, which were also devoid of megafauna [*Lance et al*., 1998].

The extensive thickets of siboglinid tubeworms require a steady supply of either methane or sulfide to survive. Anaerobic oxidation of methane generates sulfide around methane seeps [*Reeburgh*, 2007]. Thus, a sustained flux of methane to the seafloor will support the existence of widespread siboglinid tubeworms colonies. However, the siboglinid tubeworms colonies are absent on the young flows, which are presumably the sites of the most vigorous upward methane flux. Conversely, they are abundant on the surface of old flows. These observations suggest that a biological succession is occurring. Initially, the flows are devoid of even mobile taxa as they are too young to have recruited and grown into colonies. Mobile organisms will become the first occupants of these fresh flows and with time sessile organisms recolonize the seafloor surface. Where a supply of methane persists, communities of siboglinid worms will colonize the surface and flourish. The progressive dewatering and degassing of methane from episodic flows, spread through the plateau surface will result in a regular supply of methane and/or sulfide to support the bacteria within the siboglinid tubeworms.

5. Summary and Conclusions

Sediment cores, ROV dives, and detailed AUV mapping surveys provide insight into the ongoing processes that have generated large low-relief mud volcanoes on the slope of the Canadian Beaufort Sea at ~282, ~420, and ~740 m water depths. The circular structures observed at these sites are formed by the ongoing accumulation of mud on the seafloor as overpressured biogenic methane expels warm fluidized sediment

from the subsurface. The low-chlorinity and sodium-rich fluid with negative $\delta^{18}O$ and δD values is inferred to result from mixtures of seawater, Arctic meteoric water, and water from clay dehydration at $\geq$750 m subsurface depths. There is evidence for gas hydrate presence at the three sites but its stability is probably limited to a thin zone near the seafloor because ascending fluids are warmer than bottom ocean waters.

Side scan surveys allow the identification of recent flows. Young flows, devoid of any sessile colonization, experience degassing and their backscatter intensity changes from high to low. As degassing proceeds, sediment viscosity increase and flows consolidate. The low relief observed atop the mud volcanoes plateaus results from the ponding of low-viscosity sediment whereas the steep flanks are formed by more viscous degassed sediment dribbling downslope. The appearance of fresh flows and the ROV observations of bubbling gas indicate this is a dynamic environment still experiencing eruptions. Areas atop the mud volcanoes not affected by recent eruptions are colonized by extensive communities of siboglinid tubeworms, which are the first living chemosynthetic biological communities discovered on the continental margins in the Western Arctic.

Acknowledgments
Support was provided by the Geological Survey of Canada, Department of Fisheries and Oceanography, David and Lucile Packard Foundation, ArcticNet Programme, and the Korea Polar Research Institute (grant PE15061). Comments from Edward King, Jerry Dickens, and an anonymous reviewer greatly improved the manuscript. Data supporting Figures 4 and 5 are available in supporting information Tables S1 and S2. Video clips illustrating ROV observations are available at http://www.mbari.org/arctic_shelf_edge.

References

Barnard, A., W. W. Sager, J. E. Snow, and M. D. Max (2015), Subsea gas emissions from Barbados accretionary complex, *Mar. Pet. Geol.*, *64*, 31–42.

Blasco, S., et al. (2013), State of knowledge: Beaufort Sea seabed geohazards associated with offshore hydrocarbon development, *Geol. Surv. Can. Open File Rep.*, *6989*, p. 307.

Blasco, S. M., G. Fortin, P. R. Hill, M. J. O'Connor, and J. Brigham-Grette (1990), The late Neogene and quaternary stratigraphy of the Canadian Beaufort continental shelf, in *The Geology of North America*, edited by A. Grantz, L. Johnson, and J. F. Sweeney, vol. 50, pp. 491–502, Geol. Soc. Amer., Boulder, Colo.

Boetius, A., K. Ravenschlag, C. J. Schubert, D. Rickert, F. Widdel, A. Gieseke, R. Amann, B. B. Jørgensen, U. Witte, and O. Pfannkuche (2000), A marine microbial consortium apparently mediating anaerobic oxidation of methane, *Nature*, *407*, 623–626.

Brewer, P. G., F. M. Orr Jr., G. Friederich, K. A. Kvenvolden, D. L. Orange, J. McFarlane, and W. Kirkwood (1997), Deep ocean field test of methane hydrate formation, *Geology*, *25*, 407–410.

Brown, K. M., D. M. Saffer, and B. A. Bekins (2001), Smectite diagenesis, pore-water freshening, and fluid flow at the toe of the Nankai wedge, *Earth Planet. Sci. Lett.*, *194*, 97–109.

Buatier, M. D., D. R. Peacor, and J. R. O'Neil (1992), Smectite-illite transition in Barbados accretionary wedge sediments: TEM and AEM evidence for dissolution/crystallization at low temperature, *Clays Clay Miner.*, *40*, 65–80.

Caress, D. W., and D. N. Chayes (1996), Improved processing of hydrosweep DS multibeam data on the R/V Maurice Ewing, *Mar. Geophys. Res.*, *18*, 631–650.

Caress, D. W., H. Thomas, W. J. Kirkwood, R. McEwen, R. Henthorn, D. A. Clague, C. K. Paull, J. Paduan, and K. L. Maier (2008), High-resolution multibeam, sidescan, and subbottom surveys using the MBARI AUV D. Allan B, in Marine Habitat Mapping Technology for Alaska: Alaska Sea Grant College Program, edited by J. R. Reynolds and H. G. Greene, Univ. Alaska Fairbanks, pp. 47–69, Alaska Sea Grant for North Pacific Research Board, Fairbanks, Alaska, doi:10.4027/mhmta.2008.04.

Chao, H.-C., C.-F. You, H.-C. Liu, and C.-H. Chung (2013), The origin and migration of mud volcano fluids in Taiwan: Evidence from hydrogen, oxygen, and strontium isotopes, *Geochim. Cosmochim. Acta*, *114*, 29–51.

Claypool, G. E., B. J. Presley, and I. R. Kaplan (1973), Gas analyses in sediment samples from legs 10, 11, 13, 14, 15, 18 and 19, *Initial Rep. Deep Sea Drill. Proj.*, *19*, 879–884.

Cook, F. A., K. C. Coflin, L. S. Lane, J. R. Dietrich, and J. Dixon (1987), Structure of the southeast margin of the Beaufort–Mackenzie Basin, Arctic Canada, from crustal seismic-reflection data, *Geology*, *15*, 931–935.

Dählmann, A., and G. J. de Lange (2003), Fluid-sediment interactions at eastern Mediterranean mud volcanoes: A stable isotope study from ODP Leg 160, *Earth Planet. Sci. Lett.*, *212*, 377–391.

de Beer, D., E. Sauter, H. Niemann, N. Kaul, J.-P. Foucher, U. Witte, M. Schlüter, and A. Boetius (2006), In situ fluxes and zonation of microbial activity in surface sediments of the Håkon Mosby mud volcano, *Limnol. Oceanogr. Methods*, *52*, 1315–1331.

Dia, A. N., M. Castrec-Rouelle, J. Boulègue, and P. Comeau (1999), Trinidad mud volcanoes: Where do the expelled fluids come from?, *Geochim. Cosmochim. Acta*, *63*, 1023–1038.

Dickens, G. R., M. Koelling, D. C. Smith, L. Schnieders, and IODP Expedition 302 Scientists (2007), Rhizon sampling of sore waters on scientific drilling expeditions: An example from the IODP expedition 302, Arctic Coring Expedition (ACEX), *Sci. Drill.*, *4*, 22–25.

Dimitrov, L. I. (2002), Mud volcanoes—The most important pathway for degassing deeply buried sediments, *Earth Sci. Rev.*, *59*, 49–76.

Dixon, J. (1993), Geological Atlas of the Beaufort-Mackenzie area, *Geol. Surv. Can. Misc. Rep.*, *59*, 173 pp.

Etiope, G., and A. V. Milkov (2004), A new estimate of global methane flux from onshore and shallow submarine mud volcanoes to the atmosphere, *Environ. Geol.*, *46*, 997–1002.

Feseker, T., J.-P. Foucher, and F. Harmegnies (2008), Fluid flow or mud eruptions? Sediment temperature distributions on Håkon Mosby mud volcano, SW Barents Sea slope, *Mar. Geol.*, *247*, 194–207.

Feseker, T., A. Dahlmann, J.-P. Foucher, and F. Harmegnies (2009a), In-situ sediment temperature measurements and geochemical pore-water data suggest highly dynamic fluid flow at Isis mud volcano, eastern Mediterranean Sea, *Mar. Geol.*, *261*, 128–137.

Feseker, T., T. Pape, K. Wallmann, S. A. Klapp, F. Schmidt-Schierdhorn, and G. Bohramnn (2009b), The thermal structure of the Dvurechensikii mud volcano and its implications for gas hydrate stability and eruption dynamics, *Mar. Pet. Geol.*, *26*, 1812–1823.

Feseker, T., A. Boetius, F. Wenzhöfer, J. Blandin, K. Olu, D. R. Yoeger, R. Camillli, C. R. German, and D. de Beer (2014), Eruption of a deep-sea mud volcano triggers rapid sediment movement, *Nat. Commun.*, *5*, 5385, doi:10.1038/ncomms6385.

Foucher, J.-P., S. Dupre´, C. Scalabrin, T. Feseker, F. Harmegnies, and H. Nouze´ (2010), Changes in seabed morphology, mud temperature and free gas venting at the Håkon Mosby mud volcano, offshore northern Norway, over the time period 2003–2006, *Geo Mar. Lett.*, *30*, 157–167.

Frederick, J. M., and B. A. Buffett (2015), Taliks in relict submarine permafrost and methane hydrate deposits: Pathways for gas hydrate escape under present and future conditions, *J. Geophys. Res. Earth Surf.*, *119*, 106–122, doi:10.1002/2013JF002987.
Freed, R. L., and D. R. Peacor (1989), Variability in temperature of smectite/illite reaction in Gulf Coast sediments, *Clay Miner.*, *24*, 171–180.
Godon, A., N. Jendrzejewski, M. Castrec-Rouelle, A. Dia, F. Pineau, J. Boulègue, and M. Javoy (2004), Origin and evolution of fluids from mud volcanoes in the Barbados accretionary complex, *Geochim. Cosmochim. Acta*, *68*, 2153–2165.
Haeckel, M., B. P. Boudreau, and K. Wallmann (2007), Bubble-induced porewater mixing: A 3-D model for deep porewater irrigation, *Geochim. Cosmochim. Acta*, *71*, 5135–5154.
Hensen, C., K. Wallmann, M. Schmidt, C. R. Ranero, and E. Suess (2004), Fluid expulsion related to mud extrusion off Costa Rica—A window to the subducting slab, *Geology*, *32*, 201–204.
Hoffman, J., and J. Hower (1979), Clay mineral assemblages as low grade metamorphic geothermometers: Application to the thrust faulted disturbed belt of Montana, U.S.A., in *Aspects of Diagenesis*, edited by P. A. Scholle and P. S. Schluger, *Spec. Publ. Soc. Econ. Paleontol. Mineral.*, 26, 55–79.
Holmes, R. M., J. W. McClelland, B. J. Peterson, I. A. Shiklomanov, A. I. Shiklomanov, A. V. Zhulidov, V. V. Gordeev, and N. N. Bobrovitskaya (2002), A circumpolar perspective on fluvial sediment flux to the Arctic Ocean, *Global Biogeochem. Cycles*, *16*(4), 1098, doi:10.1029/2001GB001849.
Hunt, J. M. (1996), *Petroleum Geochemistry and Geology*, 743 pp., W. H. Freeman, N. Y.
Jennings, S., and G. R. Thompson (1986), Diagenesis of Plio-Pleistocene sediments of the Colorado River Delta, southern California, *J. Sediment. Res.*, *56*, 89–98.
Jin, Y. K., et al. (2015), Overview of field operation during a 2013 research expedition to the southern Beaufort Sea on the *R/V Araon*, *Geol. Surv. Can. Open File Rep.*, *7754*, p. 181, doi:10.4095/295856.
Kastner, M., H. Elderfield, W. J. Jenkins, J. M. Gieskes, and T. Gamo (1993), Geochemical and isotopic evidence for fluid in the western Nankai subduction zone, Japan, in *Proceedings of the Ocean Drilling Program Scientific Reports*, vol. 131, edited by I. Hill, A. Taira, and J. V. Firth, pp. 397–413, Ocean Drill. Program, College Station, Tex.
Ko, J. (1992), Illite/smectite diagenesis in the Beaufort-Mackenzie Basin Arctic Canada, PhD dissertation, p. 192, McGill Univ., Montreal, Que., Canada.
Ko, J., and R. Hesse (1998), Illite/smectite diagenesis in the Beaufort-Mackenzie Basin, Arctic Canada: Relation to hydrocarbon occurrence?, *Bull. Can. Pet. Geol.*, *46*, 174–188.
Kopf, A. J. (2002), Significance of mud volcanism, *Rev. Geophys.*, *40*(2), 1005, doi:10.1029/2000RG000093.
Lacelle, D. (2011), On the $\delta^{18}O$, δD, and D-excess relations in meteoric precipitation and during equilibrium freezing: Theoretical approach and field experiments, *Permafrost Periglacial Processes*, *22*, 13–25.
Lance, S., P. Henry, X. Le Pichon, S. Lallemant, H. Chamley, F. Rostek, J.-C. Faugeres, E. Gonthier, and K. Olu (1998), Submersible study of mud volcanoes seaward of the Barbados accretionary wedge: Sedimentology, structure and rheology, *Mar. Geol.*, *145*(3–4), 255–292.
Lapham, L. L., R. M. Wilson, I. R. McDonald, and J. P. Chanton (2014), Gas hydrate dissolution rates quantified with laboratory and seafloor experiments, *Geochim. Cosmochim. Acta*, *125*, 492–503.
Lawrence, J. R., J. M. Gieskes, and W. S. Broecker (1975), Oxygen isotope and cation composition of DSDP pore waters and the alteration of layer II basalts, *Earth Planet. Sci. Lett.*, *27*, 1–10.
Li, N., H. Huang, and D. Chen (2014), Fluid sources and chemical processes inferred from geochemistry of pore fluids and sediments of mud volcanoes in the southern margin of the Junggar Basin, Xinjiang, northwestern China, *Appl. Geochem.*, *46*, 1–9.
Lösekann, T., A. Robador, H. Niemann, K. Knittel, A. Boetius, and N. Dubilier (2008), Endosymbioses between bacteria and deep-sea siboglinid tubeworms from an Arctic Cold Seep (Håkon Mosby Mud Volcano, Barents Sea), *Environ. Microbiol.*, *10*, 3237–3254.
Mackay, J. R., and S. R. Dallimore (1992), Massive ice of the Tuktoyaktuk area, western Arctic coast, Canada, *Can. J. Earth Sci.*, *29*, 1235–1249.
Mazzini, A., H. Svensen, G. G. Akhmanov, G. Aloisi, S. Planke, A. Malthe-Sorenssen, and B. Istadi (2007), Triggering and dynamic evolution of the LUSI mud volcano, Indonesia, *Earth Planet. Sci. Lett.*, *261*, 375–388.
Mazzini, A., H. Svensen, S. Planke, I. Guliyev, G. G. Akhmanov, T. Fallik, and D. Banks (2009), When mud volcanoes sleep: Insight from seep geochemistry at the Dashgil mud volcano, Azerbaijan, *Mar. Pet. Geol.*, *26*, 1704–1715.
McLaughlin, F. A., E. C. Carmack, R. W. Macdonald, H. Melling, J. H. Swift, P. A. Wheeler, B. F. Sherr, and E. B. Sherr (2004), The joint roles of Pacific and Atlantic-origin waters in the Canada Basin, 1997–1998, *Deep Sea Res., Part I*, *51*, 107–128.
Michel, F. A. (1986), Hydrogeology of the central Mackenzie Valley, *J. Hydrol.*, *85*, 379–405.
Michel, F. A. (2011), Isotope characterization of the ground ice in Northern Canada, *Permafrost Periglacial Processes*, *22*, 3–12.
Milkov, A. V. (2000), Worldwide distribution of submarine mud volcanoes and associated gas hydrates, *Mar. Geol.*, *167*, 29–42.
Moorman, B. J., F. A. Michel, and R. J. Drimmie (1996), Isotopic variability in Arctic precipitation as a climatic indicator, *Geosci. Can.*, *23*, 189–194.
Olu-Le Roy, K., M. Sibuet, A. Fiala-Médioni, S. Gofas, C. Salas, A. Mariotti, J.-P. Foucher, and J. Woodside (2004), Cold seep communities in the deep eastern Mediterranean Sea: Composition, symbiosis and spatial distribution on mud volcanoes, *Deep Sea Res., Part I*, *51*, 1915–1936.
Paull, C. K., and W. Ussler (2001), History and significance of gas sampling during the DSDP and ODP drilling associated with gas hydrates, in *Natural Gas Hydrates: Occurrence, Distribution and Detection*, vol. 124, edited by C. K. Paull and W. P. Dillon, pp. 53–66, AGU, Washington, D. C.
Paull, C. K., A. J. T. Jull, L. J. Toolin, and T. Linick (1985), Stable isotopic evidence for chemosynthesis in an abyssal seep community, *Nature*, *315*, 709–711.
Paull, C. K., C. S. Martens, J. Chanton, A. C. Neumann, J. Coston, A. T. Jull, and L. T. Toolin (1989), Old carbon in living organisms and young $CaCO_3$ cements from abyssal brine seeps, *Nature*, *342*, 166–168.
Paull, C. K., et al. (2011), Tracking the decomposition of permafrost and gas hydrate under the shelf and slope of the Beaufort Sea, in *Proceedings of the 7th International Conference on Gas Hydrate*, *5581*, 12, Edinburgh, Scotland.
Paull, C. K., D. W. Caress, H. Thomas, E. Lundsten, K. Anderson, R. Gwiazda, M. Riedel, M. McGann, and J. C. Herguera (2015), Seafloor geomorphic manifestations of gas venting and shallow sub-bottom gas hydrate occurrences, *Geospheres*, *11*, 491–513.
Pelletier, B. R. (1987), Marine science atlas of the Beaufort Sea: Geology and geophysics, *Geol. Surv. Can. Misc. Rep.*, *40*, 39 pp., doi:10.4095/126940.
Piñero, E., E. Gràcia, F. Martínez-Ruiz, J. C. Larrasoaña, A. Vizcaíno, and G. Ercilla (2007), Gas hydrate disturbance fabrics of southern Hydrate Ridge sediments (ODP Leg 204): Relationship with texture and physical properties, *Geo Mar. Lett.*, *27*, 279–288, doi:10.1007/s00367-007-0077-z.

Pohlman, J., T. D. Lorenson, P. E. Hart, C. D. Ruppel, C. Joseph, M. E. Torres, and B. D. Edwards (2011), Evidence for freshwater discharge at a gas hydrate-bearing seafloor mound on the Beaufort Sea continental slope, Abstract GC41B-0813 presented at 2011 Fall Meeting, AGU, San Francisco, Calif.

Quigley, T., and A., Mackenzie (1988), The temperatures of oil and gas formation in the sub-surface, *Nature*, *333*, 549–552.

Reeburgh, W. S. (2007), Oceanic methane biogeochemistry, *Chem. Rev.*, *107*, 486–513.

Reitz, A., T. Pape, M. Haeckel, M. Schmidt, U. Berner, F. Scholz, V. Liebetrau, G. Aloisi, S. M. Weise, and K. Wallmann (2011), Sources of fluids and gases expelled at cold seeps offshore Georgia, eastern Black Sea, *Geochim. Cosmochim. Acta*, *68*, 3250–3268.

Riedel, M., H. Villinger, K. ABoff, N. Kaul, and S. R. Dallimore (2014), Temperature measurements and thermal gradient estimates on the slope and shelf-edge region of the Beaufort Sea, Canada, *Geol. Surv. Can. Open File Rep.*, *7725*, p. 139, doi:10.4095/296570.

Saint-Ange, F., P. Kuus, S. Blasco, D. J. W. Piper, J. Hughes-Clarke, and K. MacKillop (2014), Multiple failure styles related to shallow gas and fluid venting, upper slope Canadian Beaufort Sea, northern Canada, *Mar. Geol.*, *355*, 136–149.

Sauter, E. J., S. I. Muyakshin, J.-L. Charlou, S. Schlüter, A. Boetius, K. Jerosch, E. Damm, J.-P. Foucher, and M. Klages (2006), Methane discharge from a deep-sea submarine mud volcano into the upper water column by gas hydrate-coated methane bubbles, *Earth Planet. Sci. Lett.*, *243*, 354–365.

Schlining, B. M., and N. J. Stout (2006), MBARI's video annotation and reference system, paper presented at Proceedings of the Marine Technology Society/Institute of Electrical and Electronics Engineers Oceans Conference, Boston, Mass., doi:10.1109/OCEANS.2006.306879.

Schrum, H. S., R. S. Murray, and B. Gribsholt (2012), Comparision of rhizon sampling and whole round squeezing for marine sediment porewater, *Sci. Drill.*, *13*, 47–50, doi:10.2204/iodp.sd.13.08.2011.

Sheppard, S. M. F., and H. A. Gilg (1996), Stable isotope geochemistry of clay minerals, *Clay Miner.*, *31*, 1–24.

Sibuet, M., and K. Olu (1998), Biogeography, biodiversity, and fluid dependence of deep-sea cold-seep communities at active and passive margins, *Deep Sea Res., Part II*, *45*, 517–567.

Sloan, E. D., and C. A. Koh (2008), *Clathrate Hydrates of Natural Gases*, 3rd ed., CRC Press, Boca Raton, Fla.

Taylor, A. E., S. R. Dallimore, P. R. Hill, E. R. Issler, S. Blasco, and F. Wright (2013), Numerical model of the geothermal regime on the Beaufort Shelf, arctic Canada since the Last Interglacial, *J. Geophys. Res. Earth Surf.*, *118*, 2365–2379, doi:10.1002/2013JF002859.

Tomaru, H., M. E. Torres, R. Matsumoto, and W. S. Borowski (2006), Effect of massive gas hydrate formation on the water isotopic fractionation of the gas hydrate system at Hydrate Ridge, Cascadia margin, offshore Oregon, *Geochem. Geophys. Geosyst.*, *7*, Q10001, doi:10.1029/2005GC001207.

Ussler, W., III, and C. K. Paull (2007), Rates and consequences of anaerobic oxidation of methane and authigenic carbonate precipitation in deep-sea sediments inferred from porewater chemical profiles, *Earth Planet. Sci. Lett.*, *226*, 271–287.

Velde, B., and G. Vasseur (1992), Estimation of the diagenetic smectite to illite transformation in time-temperature space, *Am. Mineral.*, *77*, 967–976.

von Deimling, J. S., J. Greinert, N. Chapman, W. Rabbel, and P. Linke (2010), Acoustic imaging of natural gas seepage in the North Sea: Sensing bubbles under control of variable currents, *Limnol. Oceanogr. Methods*, *8*, 155–171.

Vrijenhoek, R. C., S. B. Johnson, and G. W. Rouse (2009), A remarkable diversity of bone-eating worms (*Osedax*: Siboglinidae; Annelida), *BMC Biol.*, *7*, 74.

Weaver, J. S., and J. M. Stewart (1982), In situ hydrates under the Beaufort Sea Shelf, in *Proceedings of Fourth Canadian Permafrost Conference*, edited by H. M. French, pp. 312–319, Natl. Res. Counc. Can., Ottawa.

Werne, J. P., R. R. Haese, T. Zitter, G. Aloisi, I. Bouloubassi, S. Heijs, A. Fiala-Medioni, R. D. Pancost, J. S. Sinninghe Damste, and G. de Lange (2004), Life at cold seeps: A synthesis of biogeochemical and ecological data from Kazan mud volcano, eastern Mediterranean sea, *Chem. Geol.*, *205*, 367–390.

Whiticar, M. J. (1994), Correlation of natural gases with their source, in *The Petroleum System—From Source to Trap*, edited by L. B. Magoon and W. G. Dow, *AAPG Mem.*, 60, 261–283.

You, C. F., J. M. Gieskes, T. Lee, T. F. Yui, and H. W. Chen (2004), Geochemistry of mud volcano fluids in the Taiwan accretionary prism, *Appl. Geochem.*, *19*, 695–707.

Zoporowski, A., and S. A. Miller (2009), Modeling eruption cycles and decay of mud volcanoes, *Mar. Pet. Geol.*, *26*, 1897–1887.